PERFORMANCE OF COMPRESSED SENSING BASED IMAGE RECONSTRUCTION FOR PHOTOACOUSTIC IMAGING

A THESIS SUBMITTED TO

THE GRADUATE SCHOOL OF ENGINEERING AND SCIENCE

OF BILKENT UNIVERSITY

IN PARTIAL FULFILLMENT OF THE REQUIREMENTS FOR

THE DEGREE OF

MASTER OF SCIENCE

IN

ELECTRICAL AND ELECTRONICS ENGINEERING

By

Sadık Çağatay Çelebi

August 2022

PERFORMANCE OF COMPRESSED SENSING BASED IMAGE RECONSTRUCTION FOR PHOTOACOUSTIC IMAGING

By Sadık Çağatay Çelebi

August 2022

We certify that we have read this thesis and that in our opinion it is fully adequate, in scope and in quality, as a thesis for the degree of Master of Science.

Hayrettin Köymen (Advisor)

Emine Ülkü Sarıtaş Çukur

Behçet Murat Eyüboğlu

Approved for the Graduate School of Engineering and Sciences:

Orhan Arıkan

Director of the Graduate School

ABSTRACT

PERFORMANCE OF COMPRESSED SENSING BASED IMAGE RECONSTRUCTION FOR PHOTOACOUSTIC IMAGING

Sadık Çağatay Çelebi
M.S. in Electrical and Electronics Engineering
Supervisor: Prof. Dr. Hayrettin Köymen
August 2022

Photoacoustic Imaging (PAI) is an emerging imaging modality that provides high resolution and image contrast. PAI employs Delay-and-Sum (DAS) beamforming in which data on all array elements are processed for image reconstruction. In order to decrease system cost in PAI, it is desired to use fewer samples in image reconstruction. Reducing the number of active elements of the array without changing the aperture decreases the computational cost. However, spatial undersampling results in poor image resolution and contrast, and causes spatial artifacts called grating lobes. Compressed Sensing (CS) is a data completion scheme that alleviates the effects of undersampling using a priori knowledge of the signal of interest and the measurement scheme. We performed simulations and experiments to compare the performances of the CS image reconstruction algorithm and conventional DAS beamforming. We used Full-Width Half Maximum (FWHM) resolution and image contrast ratio (CR) as performance metrics. Simulation results offer improved image resolution and contrast when CS is used. Lateral resolution in DAS beamformed images deteriorates with depth. A lateral resolution of 150 µm is obtained regardless of depth using only a quarter of the transducer elements. However, the resolution of DAS beamformed images ranges between 255 µm to 508 µm as the depth increases. It is also shown that CS suppresses the effects of grating lobes and improves the contrast ratio up to 14 dB. We also presented the experimental verification of the results. We used an ultrasound research scanner, a tunable laser system, and an optoacoustic phantom in the experiments. We experimentally showed that the CS method mitigates the effects of spatial undersampling and outperforms the DAS beamforming method in terms of contrast by 10.81 dB on average. CS method also offers an improved lateral resolution of approximately 350 μm compared to 750 μm in DAS beamforming.

Keywords: Photoacoustic Imaging, Compressed Sensing, Delay-and-Sum Beamforming, Resolution, Full-Width Half-Maximum, Image Contrast Ratio, Signal-to-Noise Ratio

ÖZET

FOTOAKUSTİK GÖRÜNTÜLEME İÇİN SIKIŞTIRILMIŞ ALGILAMA TABANLI GÖRÜNTÜ OLUŞTURMA METODUNUN PERFORMANSI

Sadık Çağatay Çelebi
Elektrik ve Elektronik Mühendisliği, Yüksek Lisans
Tez Danışmanı: Prof. Dr. Hayrettin Köymen
Ağustos 2022

Fotoakustik Görüntüleme (FG), yüksek çözünürlük ve görüntü kontrastı sağlayan ve gelişmekte olan bir görüntüleme yöntemidir. FG'de tüm dizi dönüştürücü elemanlarındaki verilerin görüntü oluşturulması için kaydır-topla (KT) hüzme biçimlendirme tekniği kullanılır. FG'de sistem maliyetini düşürmek için görüntü yeniden yapılandırmada daha az örneklem kullanılması istenir. Dönüştürücünün açıklığını değiştirmeden dizinin aktif eleman sayısını azaltmak hesaplama maliyetini arttırmaktadır. Bununla birlikte, uzaysal seyrek örnekleme, düşük görüntü çözünürlüğü ve kontrastı ile sonuçlanır ve ızgara lobları olarak adlandırılan uzaysal artefaktlara neden olur. Sıkıştırılmış Algılama (SA) yöntemi, ilgilenilen sinyal ve ölçüm şeması hakkında önsel bilgi kullanarak alt örneklemenin etkilerini hafifleten bir veri tamamlama şemasıdır. SA görüntü oluşturma algoritması ile geleneksel KT hüzme şekillendirmesinin performanslarını karşılaştırmak için simülasyonlar ve deneyler gerçekleştirdik. Performans ölçütleri olarak Tam Genişlik Yarım Maksimum (TGYM) çözünürlük ve görüntü kontrast oranı ölçümlerini kullandık. Simülasyon sonuçları, SA kullanıldığında gelişmiş görüntü çözünürlüğü ve kontrastı sunuyor. KT hüzme biçimlendirilmiş görüntülerde yatay çözünürlük derinlikle birlikte kötüleşmektedir. Dönüştürücü elemanlarının yalnızca dörtte biri kullanılarak derinlikten bağımsız 150 μm'lik bir yanal çözünürlük elde edilir. Ancak, KT hüzme biçimlendirilmiş görüntülerin çözünürlüğü derinlik arttıkça 255 μm ila 508 μm arasında değişmektedir. Ayrıca SA'nın ızgara loblarının etkilerini bastırdığı ve kontrastı 14 dB'ye kadar iyileştirdiği gösterilmiştir. Sonuçların deneysel doğrulamasını da sunulmuştur. Deneylerde bir ultrason araştırma tarayıcısı, ayarlanabilir bir lazer sistemi ve bir fotoakustik fantom kullanılmıştır. SA yönteminin uzamsal alt örneklemenin etkilerini azalttığını ve kontrast açısından KT hüzme biçimlendirme yönteminden ortalama 10,81 dB daha iyi performans gösterdiğini deneysel olarak gösterdik. SA yöntemi ayrıca KT hüzme biçimlendirmenin sunduğu 750 µm'ye kıyasla 350 µm'lik gelişmiş bir yanal çözünürlük sunmaktadır.

Anahtar sözcükler: Fotoakustik Görüntüleme, Sıkıştırılmış Algılama, Kaydır-ve-Topla Hüzme Şekillendirme, Tam Genişlik Yarı Maksimum, Çözünürlük, Görüntü Kontrast Oranı, Sinyal-Gürüntü Oranı

Acknowledgement

I feel it is most appropriate to start by expressing my heart-felt gratitude to Professor Hayrettin Köymen. For the past two years, I have had the opportunity to learn from him, not just in the contents of this thesis, but in all areas of life. His thoughts, mannerisms, and principles quickly bled into mine. I will forever look up to his wisdom.

I would like to also thank Prof. Behçet Murat Eyüboğlu and Prof. Emine Ülkü Sarıtaş Çukur for reviewing and improving the contents of this thesis.

I extend my gratitude to my colleagues with whom I have spent countless hours in BASTA. Yasin Kumru and Akif Sinan Taşdelen have made tremendous contributions to this thesis since its inception. My work in this thesis reflects the knowledge they shared with me.

My friends, Dilge İris Girgin, Ahmet Ege Özdamar, Furkan Bertan Akgün, Onat Özder and Miraç Lütfullah Gülgönül have forever provided the support I needed during this thesis. Onat, Furkan, and Dilge were awoken in the night with my messages, asking for comfort and guidance. Ege and Miraç have given me the confidence I need before my presentations. To each and every single one, I offer my sincere apologies for the discomfort. Thank you for your patience.

I saved the last spot for those dearest to me: my always supporting sister, my loving mother, my hero father. I can never pay the debt I owe them: the opportunities they have provided me, the care they have given. Ultimately, I simply hope to be as good of a man as they want me to be.

Contents

List of Figures

List of Tables

Chapter 1

Introduction

1.1 Literature Review

Photoacoustic Imaging (PAI) is an imaging modality that combines optical illumination with Ultrasound (US) detection. PAI's ability to offer better contrast and resolution than purely optical imaging modalities in deep tissues makes it an attractive option for clinical applications [1-3].

PAI employs a natural phenomenon called the Photoacoustic (PA) effect. In PAI, a tissue sample is irradiated by modulated electromagnetic (EM) radiation to produce acoustic responses [3]. Pulsed lasers are commonly used as a source of EM radiation, but continuous-wave laser sources have also been employed [4] [5]. Optical pulsed signals within the visible and near-infrared range of the spectrum are commonly used in PAI [3]. Pulse durations are generally measured in nanoseconds, although applications of femtosecond laser pulses can be found [6,7]. As the optical signal propagates through the medium, the molecules absorb some of the signal's energy. The absorbed energy causes the tissue to heat up and rapidly expand, which is called thermoelastic expansion. Thermoelastic expansion generates acoustic waveforms called Photoacoustic (PA) waves [2,3]. PA waves can be recorded by US receivers located on the surface of the medium. PAI aims to reconstruct an optical absorption distribution map of a tissue.

PAI can be regarded as a US imaging modality that uses EM-enhanced contrast [3]. In the near-infrared region (600-900 nm wavelength), optical pulses provide high contrast and improved penetration in biological tissues [3].

Chromophores such as hemoglobin, melanin, lipids, and water in tissues are used in PAI as they are responsive to optical illumination and have different optical absorption properties [2,3,8]. In addition, optical contrast agents such as indocyanine green (ICG) [9,10] and methylene blue [11] are used for better contrast. These chromophores have been utilized in PAI for preclinical and clinical studies in fields such as vascular biology [12], oncology [13], and neurology [14]. PAI displays a greater tissue differentiation than US as optical absorption difference in these tissue types is much larger than acoustic impedance [1].

Acoustic waves experience less scattering than photons in a tissue medium, so PAI offers higher spatial resolution than purely optical systems [2,15]. Like US, spatial resolution in PAI is determined by the frequency content of the registered PA waves [1]. The bandwidth of the laser-induced PA waves is often measured in tens of MHz [16]. Such broadband signals go through frequency-selective attenuation inside a medium. High-frequency contents are usually lost due to attenuation, which limits spatial resolution [17]. PA waves coming from deep tissue regions experience more attenuation inside the tissue, so spatial resolution decreases with depth.

Photoacoustic Imaging can be divided into two categories: Photoacoustic Microscopy (PAM) and Photoacoustic Computed Tomography [18-20]. PAM reconstructs high-resolution images of medium up to a few millimeters [18] [20]. PAM is further classified based on the focusing scheme used in transmission or reception. In Optical Resolution PAM (OR-PAM), focused laser beams are used to produce PA waves, which are mechanically scanned by an US receiver. Conversely, the approach using spatially wider laser beams and detecting the PA waves by focused detectors is called Acoustic Resolution PAM (AR-PAM). A series of scans are then used to construct an image of the tissue [1,19]. In references [21,22], AR-PAM is reported to be capable of maintaining 20-50 μm lateral resolution in deep tissues. OR-PAM is capable of even higher lateral resolution, down to organelle and cellular level [23,24]. The maximum reported depths for OR-PAM and AR-PAM are 1.5 mm [25] and 11 mm [26], respectively.

Photoacoustic Computed Tomography, also called Photoacoustic Tomography (PAT), employs full-field illumination with a large diameter pulsed laser beam [1]. The resulting PA waves are then recorded on the surface by either a mechanically scanned ultrasound receiver or a fixed array of receivers. PAT's ability to image a larger and deeper area than PAM in a single pulse has made it very attractive for preclinical and clinical applications [1]. PAT has been reported to image as deep as 7 cm [27], which is significantly higher than PAM's reported maximum depths. PAT has been employed in the fields of cardiology [28], oncology [29], and breast cancer screening [30]. A PAT and US combined imaging system has also been used in the guidance of lymph node biopsy [31].

PAT can be performed in various reception scanning geometries, such as spherical, cylindrical, and planar [1]. For each geometry, a single ultrasound receiver [32] can be moved to scan the geometry, or a fitting ultrasound transducer array can be used. Ring arrays [33,34] and hemispheric arrays [30,35] can fit spherical and cylindrical geometries and are useful for imaging small animals and breast tissue [1]. Linear transducer arrays are more widely used than the other types as they are convenient, affordable, and can be operated handheld [36]. The last step of PAT is reconstructing the optical absorption distribution from received PA waves using a reconstruction algorithm [1]. Using linear or phased arrays, PAT can be applied in planar and cylindrical geometries. Like the other Computed Tomography methods, a sample is imaged at multiple viewing angles to form a 3D image by a reconstruction algorithm based on the detection geometry, such as universal back-projection [37] and time-reversal [38].

Due to similarities between US and PAI, US image reconstruction algorithms are used in PAI with some modifications [39]. One of the most commonly used algorithms is the Delay-and-Sum (DAS) beamforming [39]. DAS is simple to implement and has low computational complexity, but it also results in low resolution and high levels of sidelobes [40]. Several improvements to DAS have been proposed, such as the Delay-Multiply-and-Sum (DMAS) [40] and Double Stage Delay-Multiply-and-Sum (DS-DMAS) [41] algorithms, which have reported improvements in the dynamic range of images, but not on image resolution. Adaptive beamformers have the potential to improve image resolution. Minimum Variance (MV) beamformer, as an adaptive beamformer, has been employed in PAI [42,43], and resolution improvement was reported while the level of sidelobes was still retained.

All the beamforming algorithms mentioned are still affected by the element-to-element pitch and the full aperture of the array. Due to Shannon's theorem, if the array pitch is too large, an artifact called grating lobes appear in the reconstructed images and further decrease the image contrast and resolution [44]. The performance of DAS can be improved by using a wide transducer array with a low pitch. However, the algorithm will be more computationally exhaustive as the number of samples and array elements increases.

Compressed Sensing (CS) is a data completion scheme that deals with undersampled data [44]. The undersampling can be done in space or time. CS has been first introduced in PAI in [45] to alleviate the effects of spatial undersampling with a single ultrasound receiver in a circular scanning geometry. Since then, sparsity-based reconstruction algorithms, including CS, have been used in US [46-48] and PAT [49-55]. It is reported that CS and other sparsity-based image reconstruction algorithms improved the resolution and image contrast, and mitigated the undersampling side effects.

CS requires a model that establishes the relation between the optical absorption property of the medium and the measured PA waves. In US, this model is defined in both time [47,48] and frequency domains [46,47] analytically by solving the wave equations using Green's functions. It was shown that using CS in US imaging decreases the number of transmitted beams required for a single image and improves the frame rate for real-time US imaging.

For PAI using phased or linear transducer arrays, the model is constructed in two ways: i) using measurements from point-like objects [50,54,55] and ii) analytic solution of PA wave equation [51-53]**.** Previously proposed measurement-based models [50,54,55] involve imaging of point-like objects whose positions are known. The construction of these models is an iterative process specific to the transducer and the imaged area.

Analytically constructed models [51-53] in PAI offer a universal solution as they are not specific to the sensor equipment used or the properties of the medium. This approach resembles the time domain US forward matrices presented in [47,48], as they all involve solving wave equations using Green’s functions.

In this thesis, an optoacoustic phantom is irradiated by pulsed laser beams with a pulse duration of 5 ns. The wavelength of the laser pulses ranges between 670 nm and 820 nm. A phased array transducer is fixed on top of the phantom and is only used in reception. We did not apply any mechanical scanning. Throughout this thesis, we refer to this transmission and reception scheme as PAI. A CS-based image reconstruction algorithm is employed for PAI to remedy the effects of spatial undersampling. We performed simulations and experiments for this purpose and compared the CS-based method and DAS beamforming performances in terms of image resolution and contrast. We used DAS beamformed images as a reference.

1.2 Overview of the Thesis

The rest of this thesis is organized as follows. In Chapter 2, our experimental PAI setup and the DAS beamforming algorithm for PAI are explained. Chapter 3 focuses on presenting the CS scheme. The CS-based image reconstruction algorithm used in this thesis is presented here. The simulation and experimental results are discussed in Chapters 4 and 5, respectively. Lastly, concluding remarks and discussion are presented in Chapter 6.

Chapter 2

Photoacoustic Imaging Setup and Conventional Image Reconstruction

2.1 Photoacoustic Imaging Setup

We used an Ekspla NT352 Series Tunable Nd:YAG laser system to generate optical pulses. The pulses have a duration of 5 ns. The wavelength and energy of the optical pulses can be adjusted on the laser system. The system can produce pulses with wavelengths ranging from 660 nm to 1064 nm. The maximum energy of the beams the system can produce decreases with the wavelength of the pulses. In the system, the highest optical pulse energy used in this study is acquired at 680 nm, which is measured as 8.3 mJ. The energy levels of the optical pulses can be adjusted by a wave plate and a polarized cube beamsplitter placed at the output of the laser system.

Digital Phased Array System (DiPhAS, Fraunhofer IBMT, Frankfurt, Germany) is used to collect data. A phased array transducer operating at 7.5 MHz center frequency with 70% fractional bandwidth is used. The transducer has 128 elements with a 0.1 mm element-to-element pitch [56]. The phased array is only used in reception. We acquired samples at 80 MHz sampling frequency and recorded in parallel from all array elements for 95 μs. 35 dB constant gain is added in all measurements. The laser system operates with a trigger signal from DiPhAS. This signal ensures that the recordings by DiPhAS coincide with the optical beams.

A picture of our experimental setup is given in Figure 2.1. Optical pulses are focused into a fiberoptic cable at the laser system's output. The fiberoptic cable is mounted on the ultrasound transducer at a 45° angle. The phased array transducer and the fiberoptic cable are positioned on top of the optoacoustic phantom. In the optoacoustic phantom, a 1 mm diameter polymer tube filled with 0.5 mM ICG is positioned at 2.15 cm depth. The polymer tube has an outer diameter of 1.5 mm and an inner diameter of 0.8 mm. The thickness of the tube is 350 µm. The schematic of our experimental setup is given in Figure 2.2.

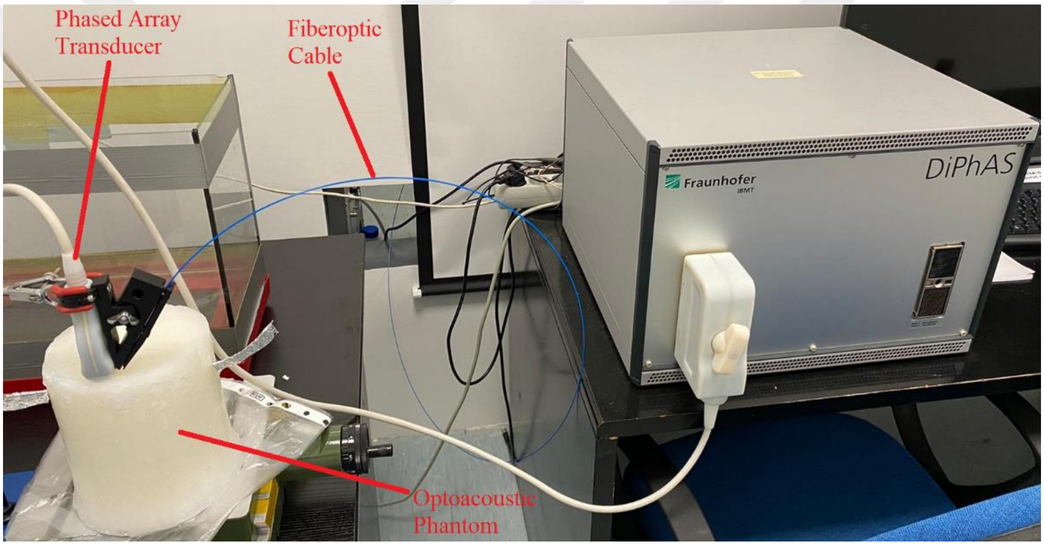

Figure 2.1: Picture of the measurement setup.

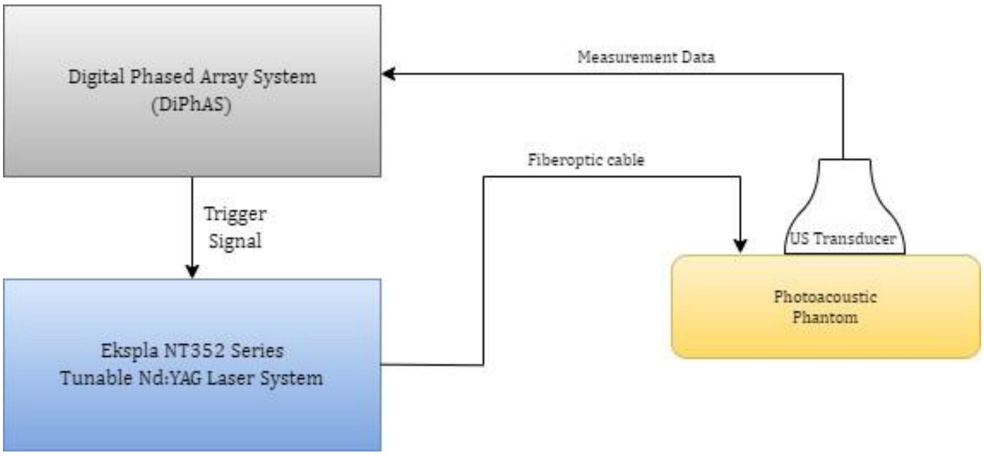

Figure 2.2: Schematic representation of the Photoacoustic Imaging Setup

In this study, we used laser pulses with five different wavelengths, 670 nm, 680 nm, 750 nm, 780 nm, and 820 nm. For each pulse wavelength, four different energy levels are used. For each wavelength and energy combination, 11 independent measurements were carried out. For signal-to-noise ratio (SNR) analysis, we also performed noise measurements without any optical illumination. Noise in each channel is recorded in these measurements.

In simulations, MATLAB toolbox “k-Wave” was used to simulate PA waves inside a medium [57]. k-Wave is capable of simulating spherical waves initiated on a defined three-dimensional grid. For the simulations, the medium’s speed of sound is adjusted to be 1450 m/s. The properties of the phased array transducer used in simulations - such as the aperture, sampling frequency, and the number of channels - are the same as the ultrasound transducer we use for experiments. For simulations, the transducer elements are assumed to be point-like.

2.2 Conventional Photoacoustic Image Formation

2.2.1 Signal Filtering of Noisy Measurements

The first step of conventional image formation is filtering the acquired data to reduce noise. The performance of the imaging algorithm is directly affected by the SNR of the measurements [58].

The signal received by the transducer array is noisy. The first source of noise is the background noise from the medium [59], which is modeled as White Gaussian [60]. Laser pulses are another noise source which usually dominate the kHz frequency range [58]. Its effect decreases at higher frequencies of the spectrum but at higher frequencies, the signal amplifier and the data acquisition card also become a source of noise [58]. By inspecting the spectra of the PA signals and noise, their frequency contents can be deduced. Later, a bandpass filter can be applied to filter out some of the noise.

For example, the power spectra of some noisy measurement data and noise measurement are given in Figure 2.3. The noisy measurement data is acquired using optical pulses with 670 nm wavelength and 8.1 mJ pulse energy. As seen from the figure, the -6 dB bandwidth of the data is 6.08 MHz and the center frequency is 4 MHz. Therefore, for the experimental measurement data we applied a bandpass filter with 1.23 MHz and 7.31 MHz cut-offs on received data and noise. The bandpass filter is a minimum-order FIR filter with a stopband attenuation of 60 dB.

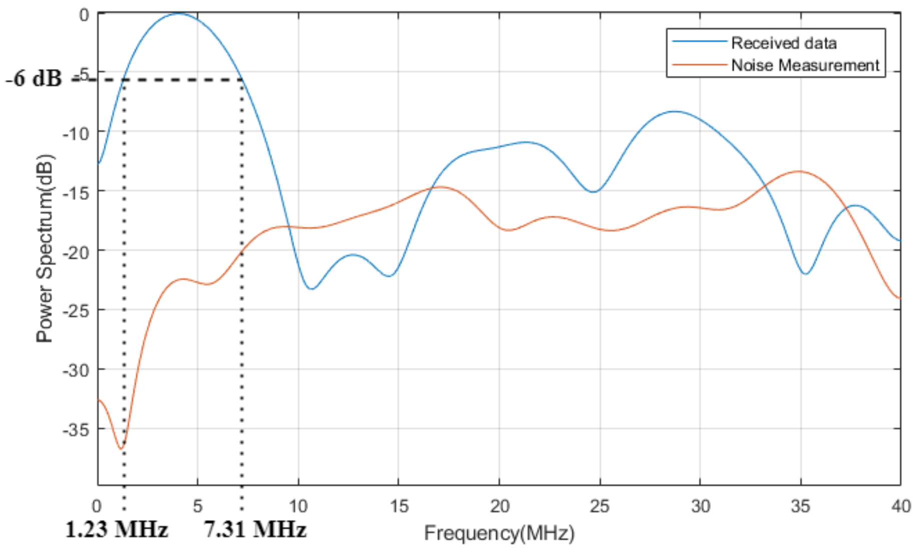

Figure 2.3: Power Spectrum Density of the measurement data and noise measurements. Optical pulses with 670 nm wavelength and 8.1 mJ pulse energy are used during measurements. No optical pulses are used during noise measurements. -6 dB bandwidth is shown on the figure with the lateral dashed lines the bandwidth cut-offs are displayed with the vertical dotted lines.

2.2.2 Delay-and-Sum Beamforming

PAI aims to create an optical absorption distribution map of the imaged area. Image reconstruction algorithms are used to create this map from the filtered measurements. Delay-and-Sum (DAS) Beamforming is the most common technique in Ultrasound and PA Imaging due to its simplicity and efficiency [41,61-64]. The first step of DAS Beamforming is forming an imaging grid, as shown in Figure 2.4.

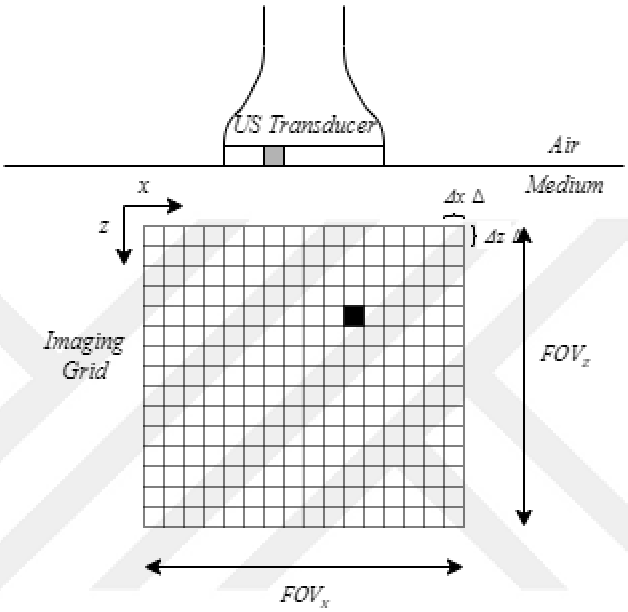

Figure 2.4: Imaging grid and transducer setup used in this thesis. A phased array transducer is positioned on a medium. The gray square represents an array element and the black square represents a grid element. Cartesian coordinates are used to represent array element and grid coordinates. x and z directions are defined as lateral and axial directions, respectively. FOV_x and FOV_z are the fields of view in these directions. Δx and Δz are pixel resolutions in x and z directions. The size of the imaging grid is $\frac{FOV_x}{\Delta x} \times \frac{FOV_z}{\Delta z}$.

The phased array is placed on the surface. We define the grid in cartesian coordinates where the center of the array corresponds to the origin. x, y and z directions correspond to lateral, elevational and axial directions respectively. Using the pitch of the array, p, and the number of elements N_{el}, the position of the center of array elements can be defined as:

$$\vec{r}_i = (x_i, y_i, z_i) = (\tfrac{p}{2}\,(2i - N_{el} - 1), 0,0) \text{ for } i = 1, \dots, N_{el}$$

where (x_i, y_i, z_i) are the position of i^{th} array element.

Delays corresponding to each pixel on the imaging grid are calculated using the positions of elements. The channel data are then shifted according to the delays, and the shifted data are summed together. The process is shown in Figure 2.5.

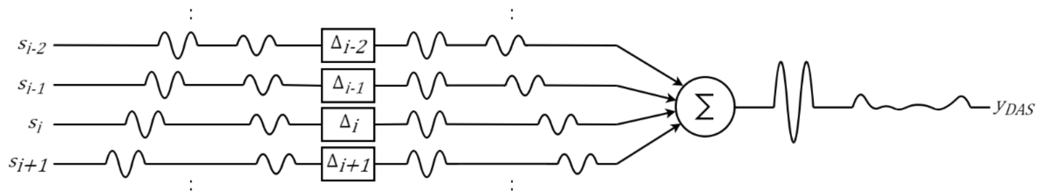

Figure 2.5: DAS Beamforming Process. Each channel contains PA signals created by two targets. After delays are applied, PA signals originating from the focused area (on-axis signals) are aligned, whereas signals from the other target (off-axis signals) are spread out. The alignment of on-axis signals causes them to sum constructively.

At time sample k and grid position r_s the reconstructed signal is given by:

$$y_{DAS}[k] = \sum_{i=1}^{N_{el}} s_i\left[k + \Delta_{i,s}\right] \tag{2.1}$$

where s_i is the received signal for channel i and $\Delta_{i,s}$ are the corresponding delays. The $\Delta_{i,s}$ is calculated as shown below.

$$\Delta_{i,s} = \frac{\sqrt{(x_i - x_s)^2 + z_s^2}}{v} f_s \tag{2.2}$$

where (x_s, y_s, z_s) are grid positions and v is the speed of sound in the medium. $y_s = 0$ for this imaging configuration. The speed of sound is assumed to be constant throughout the medium.

PAI aims to reconstruct the optical absorption distribution. Assuming that all emanating acoustic energy is due to the absorbed optical energy, the beamformed signals can be used to reconstruct an absorption map of the medium. We are interested in the initial pulse distribution (IPD) of the medium, at time sample $k = 0$. Therefore, we calculate the pulse amplitude $y_{DAS}[0]$ using beamforming on each point of the imaging grid. In the end, we end up with an image matrix that is the size of the imaging grid with each index representing the pulse amplitude at the corresponding grid location.

DAS is one of the most common image reconstruction algorithms for PA imaging [41] because of its simplicity, which allows it to be easily parallelized [61]. However, DAS also results in high levels of sidelobes, decreasing images' resolution [41]. The sidelobes are caused by the constructive overlapping of the off-axis signals [62]. Other beamforming algorithms are developed to improve resolution by decreasing the contribution of off-axis signals [41,42,62-64].

A beamformed signal that passes through the target is given in Figure 2.6(a). The presented signal is a column of the image matrix obtained after the beamforming operation. Optical pulses with 670 nm wavelength and 8.1 mJ pulse energy are used for this measurement. Due to the coherent summation of the PA waves, a pulse is observed at 22 mm depth. It is possible to further decrease the level of noise and bring out the pulse in the beamformed data by applying averaging. We performed beamforming on 11 independently taken measurements of the same setup, also using the same optical pulses, and average the beamformed data. The result of averaging operation can be seen in Figure 2.6(b). As a result of the averaging operation, the pulse is more observable.

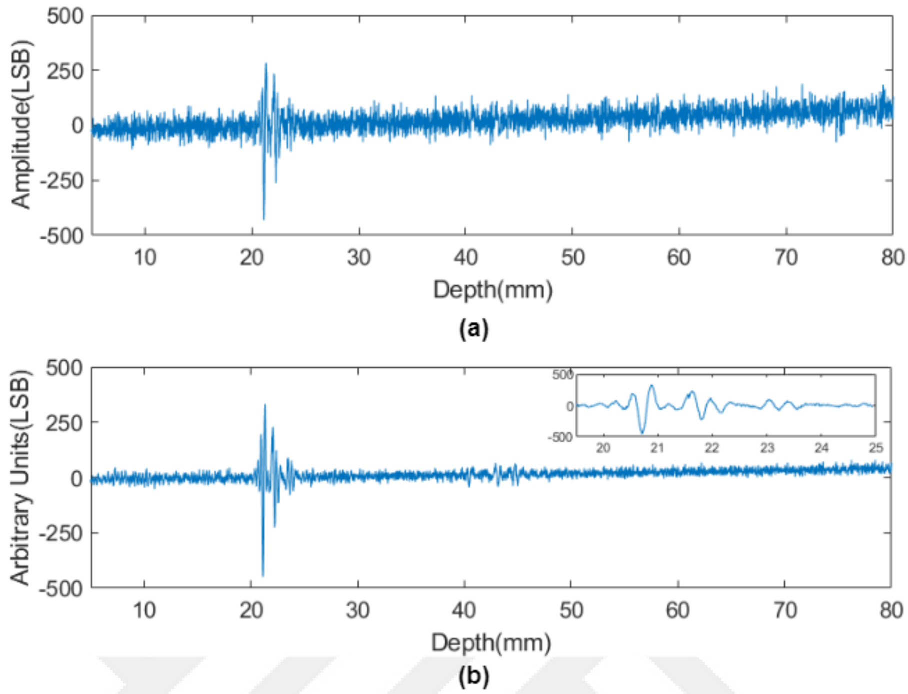

Figure 2.6. (a) Result of DAS beamforming operation applied to measurement data taken under optical pulses with 670 nm wavelength and 8.1 mJ pulse energy. (b) Beamformed signal after 11 measurement data is beamformed separately and the resulting beamformed signals are averaged. The magnitudes of signals are given in terms of the Least Significant Bits (LSB) of the Analog-to-Digital Converter of DiPhAS. The pulse is zoomed in the inset in (b).

Lastly, Hilbert transform-based envelope detection and logarithmic compression are applied to columns of the image matrix, also called scan lines. Envelope detection removes the high frequency variations of the scan lines [30]. We end up with a vector with nonnegative elements. The logarithmic compression decreases the dynamic range of the images.

2.2.3 Image Quality Metrics

We used three metrics to assess the image reconstruction performance: SNR, Full-width Half-Maximum (FWHM), and contrast. SNR represents the ratio of signal power to noise power and is measured in decibels [65]. In order to measure SNR, we performed noise measurements and processed the noise data the same way we do with signal data on each channel. The measurements we take using laser pulses contain both the PA signal (S) and some additive noise (N). We measured SNR, referred as SNR_{+1}, from DAS images as defined in Equation (2.3) [56,66].

$$\begin{aligned} SNR_{+1}(dB) &= 20\log(S+N) - 20\log(N) \\ &= 20\log\left(\frac{S+N}{N}\right) \\ &= 20\log(SNR+1) \end{aligned} \tag{2.3}$$

FWHM is used to measure resolution in both lateral and axial directions. We defined FWHM as the width of the profile – either axial or lateral - where the pulse energy drops to half of its peak value [65]. This corresponds to a 6 dB loss from the peak in log-compressed images.

Lastly, Contrast Ratio (CR) is used. A higher CR in images implies better performance of an algorithm [65]. We measured CR as given in Equation (2.4):

$$CR = 20\log\left(\frac{\mu_t}{\mu_b}\right) \tag{2.4}$$

where μ_t and μ_b are means of pixel intensities in the target region and background at the same depth.

Chapter 3

Compressed Sensing Application in Photoacoustic Imaging

3.1 Compressed Sensing

In fields that need a constant and accurate sampling of signals or images, Nyquist-Shannon's theorem is followed to avoid artifacts caused by the sampling operation [44]. By Nyquist-Shannon's sampling theorem, the sampling frequency needs to be at least twice that of the highest frequency content of the sampled signal; otherwise, the signal may not be accurately reconstructed from samples [44]. Compressed Sensing (CS) approach is developed to reduce the effect of artifacts caused by the undersampling of signals [67,68]. The missing information caused by undersampling is remedied by a list of prerequisites in formulation of the CS problem. CS can be divided into two steps: i) Defining a CS matrix that preserves the information in the measurement data and ii) Formulating a fitting recovery algorithm [67,68].

CS deals with underdetermined linear systems:

$$y_{m\times 1} = \Phi_{m\times n}\, x_{n\times 1} \tag{3.1}$$

where y is the measurement vector, x is the signal of interest, Φ is the measurement matrix or compressed sensing matrix, and $m < n$. The system described in Equation (3.1) summarizes an underdetermined linear system of equations and makes the process of recovering an $x \in \mathbb{R}^n$ ill-posed. For a given $y \in \mathbb{R}^m$ there are infinitely many x that satisfy Equation (3.1). To specify a solution among the infinitely many solutions and to ensure a decent recovery, CS relies on two principles: sparsity and incoherence [44,67,68].

3.1.1 Sparsity

Sparsity pertains to the signal of interest. One usually refers to a signal as sparse when a signal representation has only a few nonzero elements. A particular solution can be found among the many candidates by enforcing the sparsity constraint on the solution. Signal of interest may not always be sparse in the domain of intended use. In that case, a sparse signal representation can be found by transformation, e.g., Fourier [45], Wavelet [69]. In real life, many natural signals are sparse or compressible, so a sparse representation can usually be found in some domain [44]. Let $\Psi \in \mathbb{R}^{n \times n}$ be an orthonormal basis (called the sparsifying matrix) with the property:

$$f = \Psi x \tag{3.2}$$

where $f \in \mathbb{R}^n$ is the sparse representation of x under Ψ.

After the transformation of the basis, we can rewrite the expression as:

$$y = \Phi \Psi^{-1} f \tag{3.3}$$

This equation still represents an underdetermined linear system and has an infinite number of f that holds for a given y. CS recovery algorithms yield the sparsest f that we can later use to recover an x by back-transforming.

3.1.2 Incoherence

Incoherence property pertains to the sensing modality. Mutual coherence (μ) is a metric that measures the correlation between two matrices [44].

$$\mu(\Psi, \Phi) = \sqrt{n} \cdot \max_{1 \le k,j \le n} \left| \psi_k^T \phi_j \right| \tag{3.4}$$

where ϕ_j and ψ_k are k^{th} and j^{th} columns of their respective bases. Low coherence between the sparsifying and measurement matrices ensures that if a signal, f, is sparse in one domain, the measurements, y, is non-sparse in the measurement domain [70]. Measurements of a non-sparse signal are more likely to have meaningful (i.e., non-zero) samples, so low mutual coherence translates to fewer samples required for reconstruction [70].

3.2 Compressed Sensing Model Definition and Solution in PAI

While reconstructing images, it is desirable to use as few samples as possible to keep the computational intensity low. As the sampling frequency of the array used must be high [1], the number of samples can only be reduced by decreasing the number of active transducer elements. Decreasing the number of active elements without changing the aperture can introduce artifacts called grating lobes which damage resolution and contrast in the images [53].

In this section, a linear relation between our measurements, R, and the optical absorption map of the tissue, I, is established to be used in Compressed Sensing for PAI. The model presented in this section is inspired by the time domain model developed for US in [48] and the analytical model for PAI as described in [53].

The first step of model definition is establishing an imaging grid. The same imaging grid used in Section 2.2.2 is used here as well. We first discretize an area of interest with a 2D grid where each cell represents an absorber. Let the matrix $I(\vec{r})$ represent the absorption properties of these absorbers and position vector $\vec{r} = (x_s, y_s, z_s)$. The higher $I(\vec{r})$ is the more responsive it is to optical pulses. The array and grid point positions are defined similarly as in Section 2.2.2. It is assumed that the medium is homogeneous and laser light equally illuminates all absorbers, so a difference between two elements of $I(\vec{r})$ is caused purely by the difference in absorption. Let R be a matrix of size $N_{el} \times N_t$ where N_{el} is the number of channel elements and N_t is the number of time bins. Also, let I be a matrix of size $N_x \times N_z$, which is the grid's size.

We need to define a matrix K such that

$$R = KI \tag{3.5}$$

where R is vectorized version of measurement matrix (size $1 \times N_{el}N_t$), I is the vectorized version of the imaging grid (size $1 \times N_xN_z$). K has the size $N_{el}N_t \times N_xN_z$.

3.2.1 Solution of PA Wave Equation

The PA Wave Equation governs the PA wave propagation in the medium:

$$\nabla^2 p(\vec{r},t) - \frac{1}{v^2}\frac{\partial}{\partial t^2}p(\vec{r},t) = -\frac{\beta}{C_P}\frac{\partial H(\vec{r},t)}{\partial t} \tag{3.6}$$

where v_s is the speed of sound in the medium, β is the thermal coefficient of volume expansion (K^{-1}), C_P is the specific heat capacity at constant pressure and $H(\vec{r},t)$ is the heating function at position $\vec{r}$ (defined in spherical coordinates) and time t [71]. Heating function represents the thermal energy transferred to unit volume in unit time. The PA Wave Equation is a nonhomogeneous linear differential equation. The source term on the right-hand side of the expression explains that the thermoelastic expansion caused by absorption of optical pulses produce spherical acoustic waveforms. Left-hand side is a linear differential operator that is commonly used in wave equations. Finally, $p(\vec{r},t)$ is the PA wave at location $\vec{r}$ and time t.

The wave equation in Equation (3.6) can be semi-analytically solved using Green's function method [72]. In Equation (3.7), a similar nonhomogeneous wave equation is given where the source term is a point-like object in position $\vec{r} = (0,0,0)$ that produces an instantaneous response at $t = 0$.

$$\nabla^2 G(\vec{r},t) - \frac{1}{v^2}\frac{\partial}{\partial t^2}G(\vec{r},t) = -\delta(\vec{r})\delta(t) \tag{3.7}$$

The solution $G(\vec{r},t)$, called the Green's function, is the spatiotemporal impulse response (SIR) of the linear wave equation [72].

$$G(\vec{r},t) = \frac{1}{4\pi\|\vec{r}\|}\delta\left(t - \frac{\|\vec{r}\|}{v}\right) \tag{3.8}$$

Using the superposition principle, one can convert Equation (3.7) into Equation (3.6) by convolving both sides in time and position with the right-hand side of Equation (3.6):

$$\left((\nabla^2 - \frac{1}{v^2}\frac{\partial}{\partial t^2}\right) G(\vec{r},t) * S(\vec{r},t) = -\left(\delta(\vec{r})\delta(t)\right) * S(\vec{r},t) \tag{3.9}$$

where

$$S(\vec{r},t) = \frac{\beta}{C_P}\frac{\partial H(\vec{r},t)}{\partial t} \tag{3.10}$$

Under the assumption of stress confinement, the heating response to optical pulses can be separated in time and position [45]:

$$H(\vec{r},t) = \delta(t)I(\vec{r}) \tag{3.11}$$

Therefore, the solution of Equation (3.9) can be found by convolving the Green's function and the source term of PA Wave Equation

$$\begin{aligned} p(\vec{r},t) &= G(\vec{r},t) * S(\vec{r},t) \\ &= \left(\frac{1}{4\pi\|\vec{r}\|}\delta\left(t - \frac{\|\vec{r}\|}{v}\right)\right) * \left(\frac{\beta}{C_P}\frac{\partial \delta(t)}{\partial t} I(\vec{r})\right) \end{aligned} \tag{3.12}$$

The derivative of unit impulse is called the unit doublet, u_1, and has the property to differentiate a function it is convolved with.

3.2.2 Including Transducer Response

Assuming that the transducer elements are point-like, one can find the PA waves reaching the element as $p(\vec{r_i},t)$ is known. For a more accurate model, the impulse response of the transducer can be incorporated into our model. We assume that the impulse response for every element is the same, and the transfer function is modeled as a Gaussian function in the frequency domain.

$$H_{trans}(f) = \frac{1}{\sqrt{2\pi}\sigma} \exp\left(-\frac{1}{2}\frac{\left(2\pi(f - f_c)\right)^2}{\sigma^2}\right) \tag{3.13}$$

where

$$\sigma^2 = \left(\frac{bw}{100} f_c \frac{1}{2\sqrt{2\log 2}}\right)^2$$

and bw is the fractional bandwidth – expressed as a percentage – and f_c is the center frequency of the transducer.

By taking the Inverse Fourier Transform, the impulse response of the transducer elements is found as:

$$h_{trans}(t) = \cos(2\pi f_c t)\exp(-2\pi^2\sigma^2 t^2) \tag{3.14}$$

For i^{th} transducer element – located at $\vec{r_i}$ – the measurement data can analytically be expressed as the convolution of acoustic pressure on the array element and the impulse response of the transducer:

$$\begin{aligned} & R^i(t) = p(\vec{r_i}, t) * h_{trans}(t) \\ & = \int_{\vec{r}} \left(\delta\left(t - \frac{\left\|\vec{r'} - \vec{r_i}\right\|}{v}\right) * u_1(t) * h_{trans}(t)\,\right) I\left(\vec{r'}\right) \frac{\beta}{4\pi C_P \left\|\vec{r'} - \vec{r_i}\right\|} d\vec{r'} \\ & = \int_{\vec{r}} \frac{\beta}{4\pi C_P \left\|\vec{r'} - r_i\right\|} h'_{trans}\left(t - \frac{\left\|\vec{r'} - r_i\right\|}{v}\right) I\left(\vec{r'}\right) d\vec{r'} \end{aligned}$$

where

$$h'_{trans}(t) = (-2\pi f_c \sin(2\pi f_c t) - 4\pi^2\sigma^2 t\cos(2\pi f_c t))\exp(-2\pi^2\sigma^2 t^2) \tag{3.15}$$

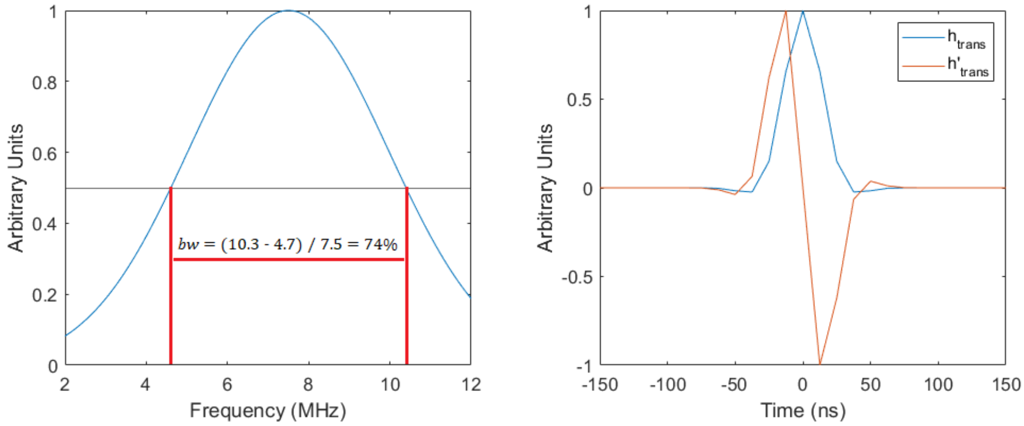

Figure 3.1: (a) the transfer function of the transducer with 7.5 MHz center frequency and 75% bandwidth. (b) impulse response of the transducer and its derivative.

By discretizing the integral kernel $\vec{r}$ with $(x, y, z) = (k\Delta x, 0, l\Delta z)$ and $t_j \in [t_0, t_{end}]$, the problem can be expressed as:

$$R^i(t_j) = \sum_{k=1}^{N_x} \sum_{l=1}^{N_z} \frac{\beta}{4\pi C_P \|r\|} h'_{trans}\left(t_j - t_0 - \frac{\|r\|}{v_s}\right) I(k\Delta x, 0, l\Delta z) \tag{3.16}$$

where $\|r\| = \sqrt{(x_i - k\Delta x)^2 + (l\Delta z)^2}$ and $(x_i, 0{,}0) = r_i$. By using smaller pixels, we can better represent the initial pulse distribution on the image.

We can rewrite Equation (3.16) as

$$R^i(t_j) = \sum_{k=1}^{N_x} \sum_{l=1}^{N_z} K(i, j, k, l)\ I(k\Delta x, l\Delta z) \tag{3.17}$$

where

$$K(i, j, k, l) = \frac{\beta}{4\pi C_P \|r\|} h'_{trans}\left(t_j - t_0 - \frac{\|r\|}{v_s}\right)$$

$K(i, j, k, l)$ corresponds to impulse response in a homogeneous medium with a point absorber at position $r_{kl} = (k\Delta x, 0, l\Delta z)$ observed at time instance t_j by i^{th}

transducer. For simplicity, we assume that $\beta = 1$ and $C_P = 1$ for the simulations and experiments. This choice does not affect the image resolution and contrast, it only adds/removes a constant on the image matrices.

By vectorizing the measurement matrix, R , and absorber matrix, I , we can generalize Equation (3.17) as:

$$R = KI$$

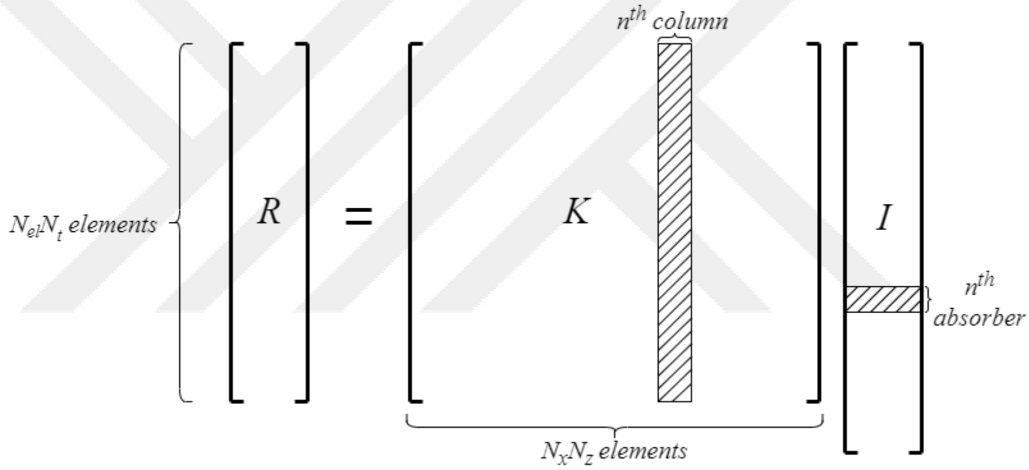

Figure 3.2. Sizes of the model used in this study. R is a vectorized version of the measurements with size $1 \times N_{el}N_t$. I is a vectorized version of the imaging grid with size $1 \times N_xN_z$. K is the forward matrix. Each element on I represents an optical absorber at a grid location. The n^{th} element, referred as the n^{th} absorber, of the I vector and the column corresponding to it on K is highlighted on the figure. A detailed view of the column is given in Figure 3.3.

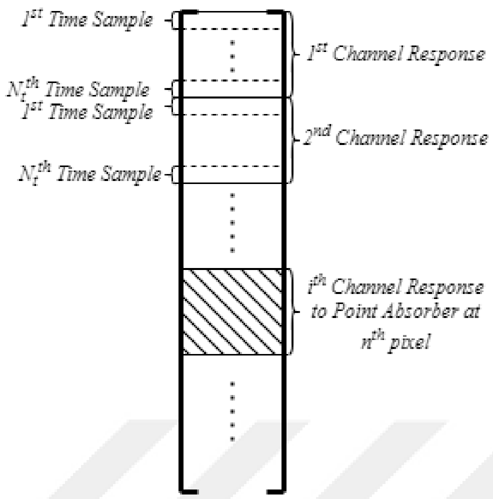

Figure 3.3: Detailed view of the n^{th} column of the K matrix. This vector represents the spatiotemporal response from an absorber located at grid location n to each element used in reconstruction. The channel responses are stacked on top of each other.

Figure 3.2 shows the sizes of R, K and A. The n^{th} entry of vector I corresponds to the absorption coefficient of an absorber at a grid location n. The corresponding column of K is the theoretic response that is measured by all elements in time and space to the n^{th} absorber. The column can be seen in detail in Figure 3.3. The channel responses are stacked on top of each other. Similarly, the measurement vector R is data recorded by each transducer stacked on top of each other. Each row of K represents the response generated by all absorbers at a particular transducer element and time instance.

The model must satisfy the sparsity and incoherence requirements discussed in Section 3.1. In PAI, absorption distribution or energy deposition intrinsically own sparsity in the spatial domain [53]. Since the images we want to reconstruct are often considered sparse, we do not require a sparsifying transformation (Ψ is the identity matrix). This requirement can also be imposed in the recovery algorithm, discussed in Section 3.2.3.

Without a sparsification matrix, we only need the measurement matrix (K) to satisfy incoherence. To satisfy incoherence, we want to maximize the number of linearly independent columns of the measurement matrix [45]. We also want the linear combinations of columns to be noise-like to ensure that one measurement of a basis vector is not correlated to the measurement of another basis vector [45]. The Transfer Point Spread Function (TPSF) is a way used in CS to assess these two conditions [45,47,48]**.** TPSF is defined as

$$TPSF(n,m) = \frac{\langle K_n, K_m \rangle}{\|K_n\| \|K_m\|}$$

where K_n and K_m are the n^{th} and m^{th} columns of K respectively. For near orthonormal matrices, TPSF is always around noise level for $n \neq m$. Limiting the maximum TPSF can satisfy the incoherence requirement [45]. In this model, columns of K corresponds to the spatial impulse response to all transducer elements from a point absorber. High TPSF is most likely to occur between neighboring pixels of our imaging grid as their spatial impulse responses are expected to be similar [48]. If the imaging grid is too fine, TPSF of two neighboring columns will unavoidably be high, and the recovery algorithm will suffer in performance. Similarly, positioning the grid too deep will increase TPSF. So, to ensure incoherence requirement, we have to sacrifice pixel resolution and maximum field-of-view.

3.2.3 Solving Model Using Compressed Sensing

Solving the linear Equation (3.5) is an iterative process. K matrix is an underdetermined matrix which is usually noninvertible. Taking the Singular Value Decomposition based pseudo-inverse of K is computationally exhausting due to the large size of K [48]. Also, due to the presence of noise in the measurements, Equation (3.5) might not have a unique solution.

To accommodate noise and the imperfections of the model, we might relax the equality constraint

$$\hat{I} = \text{argmin}_I \, \|KI - R\|_2 \tag{3.18}$$

Here we also use the l_2-norm of the residue as cost function. Equation (3.18) can yield many solutions, so to specify one, one can enforce the sparsity constraint:

$$\min\|I\|_1 \;\; subject\ to \, \|KI - R\|_2 < \epsilon \tag{3.19}$$

In the minimization problem, l_1-norm is used instead of l_2-norm as l_2-norm acts as a low-pass filter and results in poor resolution and contrast [45,49]. l_1-norm is a natural promoter of sparsity [49] and limiting l_1-norm also limits l_2-norm as well. Thus, a minimum energy and sparse solution can be found.

The convex optimization problem described in Equation (3.19) is called a Basis Pursuit Denoising (BPDN) problem [48] which we solved using a MATLAB package called SPGL1 [73,74]. Lastly, envelope detection and log compression are applied to the retrieved image matrices, I.

In our simulations and experiments, ϵ can have any value in the range of $[0, \|R\|_2]$. We defined ϵ as a factor of $\|R\|_2$ to uncouple the measurements and margin ($\epsilon = \alpha\|R\|_2$). For each image, the relaxation factor $\alpha \in [0,1]$ is chosen heuristically. We tried to keep α as low as possible to satisfy the $\|R - KI\|_2 < \alpha\|R\|_2$ constraint in the problem formulation as tightly as possible while maintaining the artifacts caused by the measurement noise and imperfections of our model to a minimum.

Chapter 4

Simulation Results

Simulations are performed to compare our model-based approach with the DAS beamformed images. Conventional beamforming has several shortcomings for this measurement setup. The lateral FWHM resolution of beamforming – not to be confused with pixel resolution, which has to do with the size of pixels – degrades with depth. DAS beamforming process introduces sidelobes and a wide mainlobe which decreases the lateral and axial resolution. Due to these, resolving two objects close to each other in images is more challenging. Finally, the undersampling in space causes artifacts of its own. We test how the CS-based algorithm performs under each of these situations through our simulations.

DAS beamformed images are created by coherent summation of measurements, whereas CS-based algorithm nonlinearly reconstructs the initial energy absorption in the tissue. The resulting CS images are lower than DAS beamformed images in terms of magnitude. In all the figures, we added appropriate constant gains to CS image matrices so that they can be fairly compared on the same scale.

4.1 Lateral and Axial Resolution

We performed a simulation to test how the Compressed Sensing algorithm compares with DAS beamforming when reconstructing images from adequately sampled data. Four point-like objects with 0.1 mm in diameter are imaged on k-Wave by a 128-element linear transducer. The center of the transducer is defined to be on $\vec{r} = (0,0,0)$. The targets are placed at $z = 2$ mm, $z = 4$ mm,

$z = 6$ mm, and $z = 8$ mm depths, respectively. The transducer has a 0.1 mm pitch and a center frequency of $f_c = 2.75$ MHz with $bw = 160\%$ fractional bandwidth. We used a sampling rate of $f_s = 80$ MHz.

The imaging grid spans $x = -1.6$ mm to $x = 1.6$ mm with 64 pixels laterally and $z = 1$ mm to $z = 9$ mm with 160 pixels axially. The pixel resolution is 50 μm in each direction. This grid is used for both DAS and CS reconstruction. The geometry of the simulation and the grid are shown on Figure 4.1. For this simulation data, we have chosen $\alpha = 0.45$ in the CS reconstruction. 95 dB constant gain is added in CS images. We used all the data from the 128 elements of the array while reconstructing the images, so no undersampling was applied.

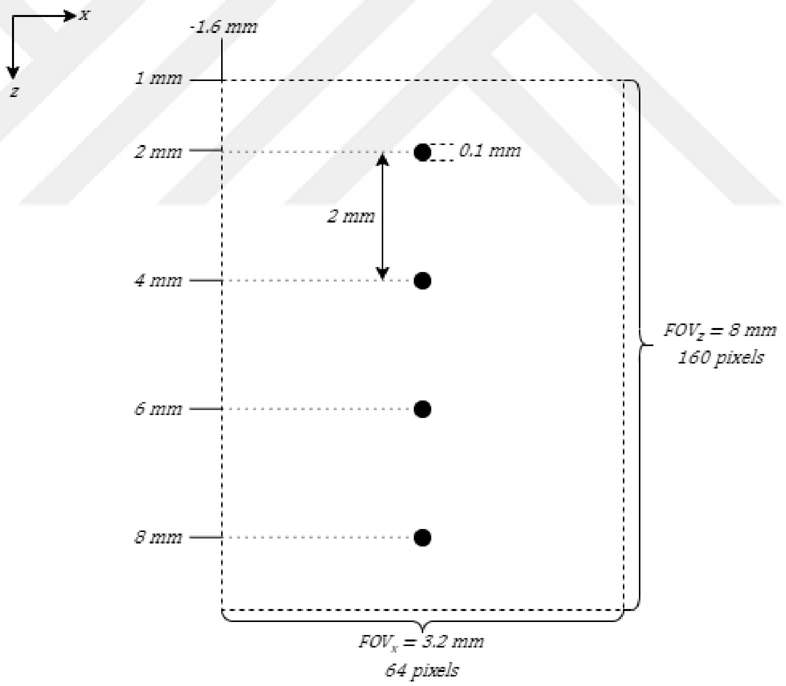

Figure 4.1. Geometry of simulation and imaging grid. Four targets (0.1 mm diameter) are placed at 2 mm, 4 mm, 6 mm, and 8 mm depths. The imaging grid spans 8 mm in axial direction and 3.2 mm in lateral directions with 160 pixels and 64 pixels respectively.

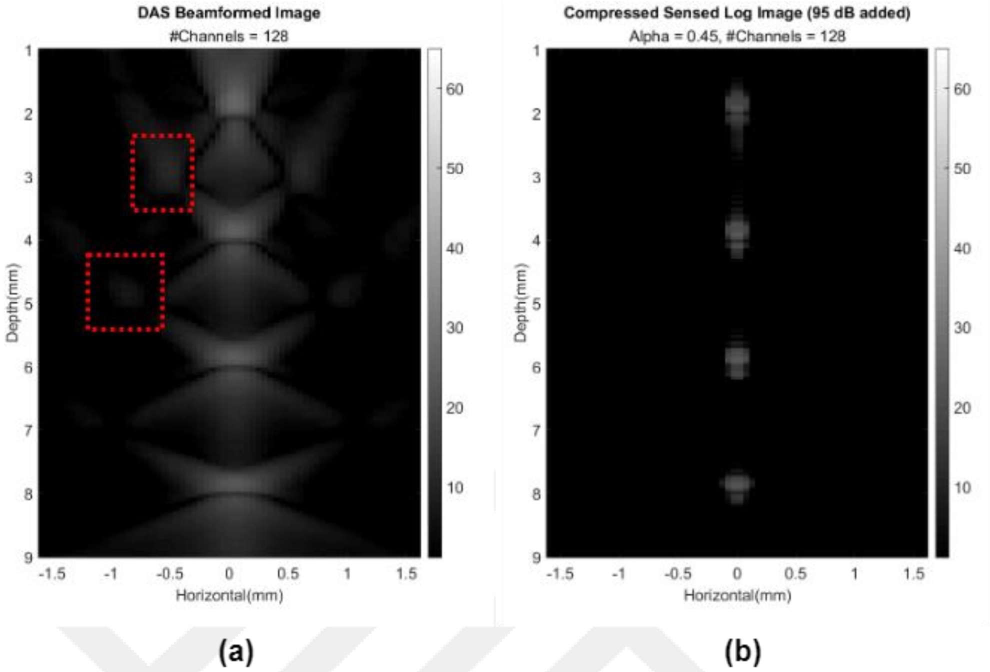

Figure 4.2: (a) DAS beamformed image with two artifacts due to mainlobes overlapping shown in dotted squares. (b) Image of targets with Compressed Sensing applied. 95 dB is added to CS images and the relaxation constant (α) is 0.45. 128 transducer elements are used in the reconstruction of both pictures.

The resulting images are given in Figure 4.2. In Figure 4.2(a), the DAS beamforming operation results in wide mainlobes. Due to the overlapping of the mainlobes, artifacts appear. Two of such artifacts are shown in dashed squares. These artifacts give the false impression that there are targets with lower absorption properties on $z = 3$ mm and $z = 5$ mm depths. In Figure 4.2(b), the images reconstructed with the CS-based method result in narrower mainlobes, so we do not observe the same artifacts.

Axial profiles of the images at targets' locations are compared in Figure 4.3 and axial resolutions for each target are given separately in Table 4.1. Figure 4.3 and Table 4.1, show that the FWHMs in the image obtained with CS are smaller than FWHM of beamformed images.

The peak pixel intensities decrease with depth in DAS beamformed image. For instance, there's a 3.4 dB drop between pixel intensities of the targets located at 2 mm and 8 mm depth even though they produce similar acoustic responses. Signals originating from 8 mm are attenuated more than signals originating from 2 mm, so a decrease between pixel intensities is observed. In the CS model, we incorporated the depth-related attenuation with Green's functions, so such a decrease is not observed in images reconstructed with CS and peak pixel intensity stays in 22.5-24 dB range.

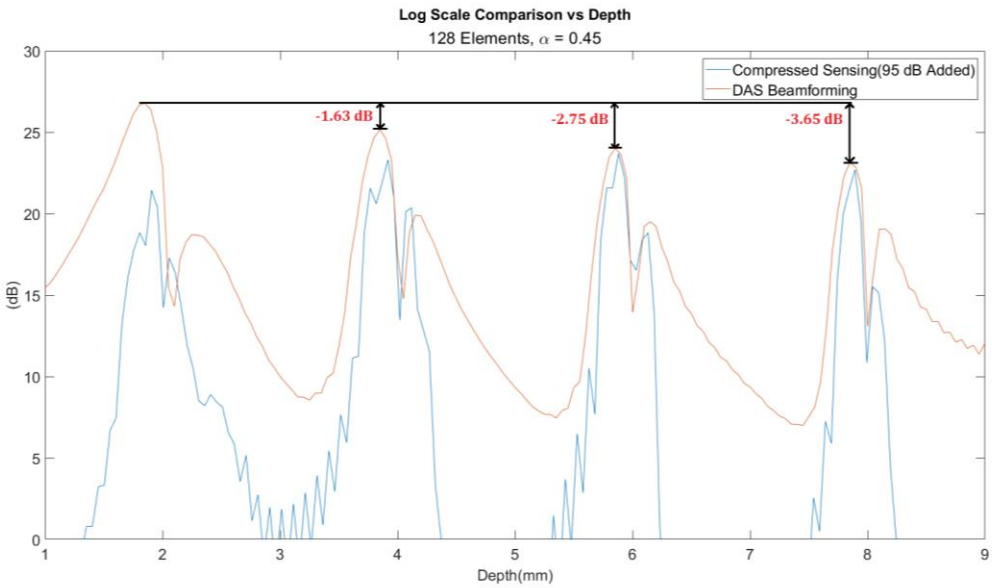

Figure 4.3: Comparison of axial profiles of DAS and CS. The targets are placed at 2 mm, 4 mm, 6 mm, and 8 mm depths. The differences between the responses of the first target and the rest are shown in the figure.

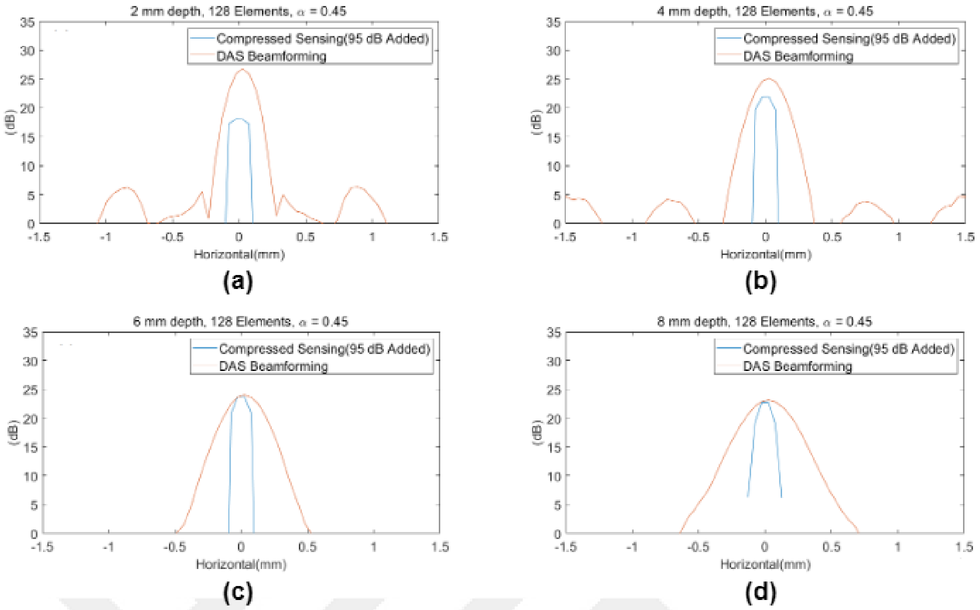

Figure 4.4: Comparison of lateral profiles of DAS and CS for targets located at (a) 2 mm depth, (b) 4 mm depth, (c) 6 mm depth, (d) 8 mm depth

In Figure 4.4, the lateral profiles of DAS beamformed and CS reconstructed images are shown. The FWHM resolutions in the lateral direction are given in Table 4.1 as well. CS-based method results in images with improved lateral resolution. The FWHM deteriorates with depth in DAS beamformed image, it doubles from 2 mm to 8 mm depth. Meanwhile, the FWHM stays approximately 160 µm in images with CS. DAS images' wider mainlobe can be seen in all plots in Figure 4.4. In Figure 4.4(a-b) the sidelobes of DAS beamformed images can also be seen.

Table 4.1. Horizontal and Lateral Resolutions of DAS and CS images for 4 targets at different depths.

Depth	DAS FWHM (Lateral)	CS FWHM (Lateral)	DAS FWHM (Axial)	CS FWHM (Axial)
2 mm	0.255 mm	0.165 mm	0.580 mm	0.438 mm
4 mm	0.325 mm	0.157 mm	0.610 mm	0.437 mm
6 mm	0.407 mm	0.156 mm	0.572 mm	0.419 mm
8 mm	0.508 mm	0.171 mm	0.555 mm	0.238 mm

Table 4.2 compares each target's image contrasts obtained from DAS and CS images. The contrast of targets with the background decreases with depth in DAS images. CS performs better in terms of contrast for all targets.

Table 4.2. Comparison of contrast ratio (CR) obtained from DAS and CS images for 4 targets at different depths.

Depth	DAS CR	CS CR
2 mm	15.96 dB	22.11 dB
4 mm	14.99 dB	23.27 dB
6 mm	13.96 dB	24.61 dB
8 mm	13.12 dB	23.42 dB

4.2 Grating Lobes

Spatial undersampling itself is responsible for artifacts. If the spacing between two consecutive elements is more than $\lambda/2$ (λ being the wavelength corresponding to the highest frequency content of PA waves), an artifact called grating lobes appears [53]. Grating lobes are spatial aliasing effects.

An absorber, placed at 4.5 mm depth, is imaged using a 128-element linear transducer with 0.1 mm pitch. The transducer has a center frequency of $f_c = 2.75$ MHz and $bw = 160\%$ fractional bandwidth. We inspected the recorded signals and saw that their spectra are between 500 kHz and 5 MHz. The highest frequency content is at 5 MHz, so $\lambda = \frac{1450\ m/s}{5\ MHz} = 290$ µm. We used a sampling frequency of $f_s = 80$ MHz.

The imaging grid spans $x = -5$ mm to $x = 5$ mm with 200 pixels laterally and $z = 3.5$ mm to $z = 6$ mm with 50 pixels axially. The pixel resolution is 50 µm in either direction. This grid is used for both DAS and CS reconstruction. The idea is to observe the grating lobes appearing on either side of the target using both methods. We only use a fraction of the elements to induce grating lobes. The aperture is kept the same in all the images. The imaging grid and the simulation geometry is given in Figure 4.5.

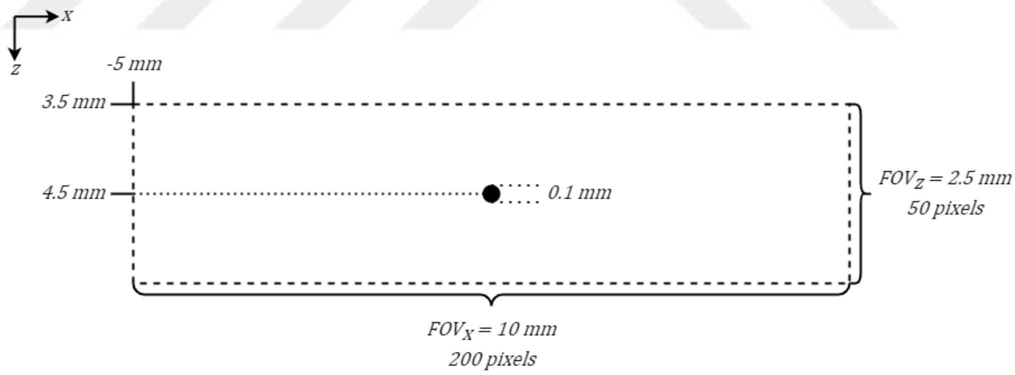

Figure 4.5. Simulation geometry and imaging grid used in image reconstruction. An absorber with 0.1 mm diameter is placed at 4.5 mm depth. The imaging grid spans 2.5 mm axially and 10 mm laterally with 50 pixels and 200 pixels, respectively.

DAS beamformed images are given in Figure 4.6. They are imaged with equally spaced 128, 32, 16, and 8 elements. The spacing between elements corresponds to 0.1, 0.4, 0.8, and 1.6 mm, respectively. The aperture is kept the same for all measurements. As the number of array elements used in reconstruction decreases, we observe a decrease in the peak pixel intensity of the image.

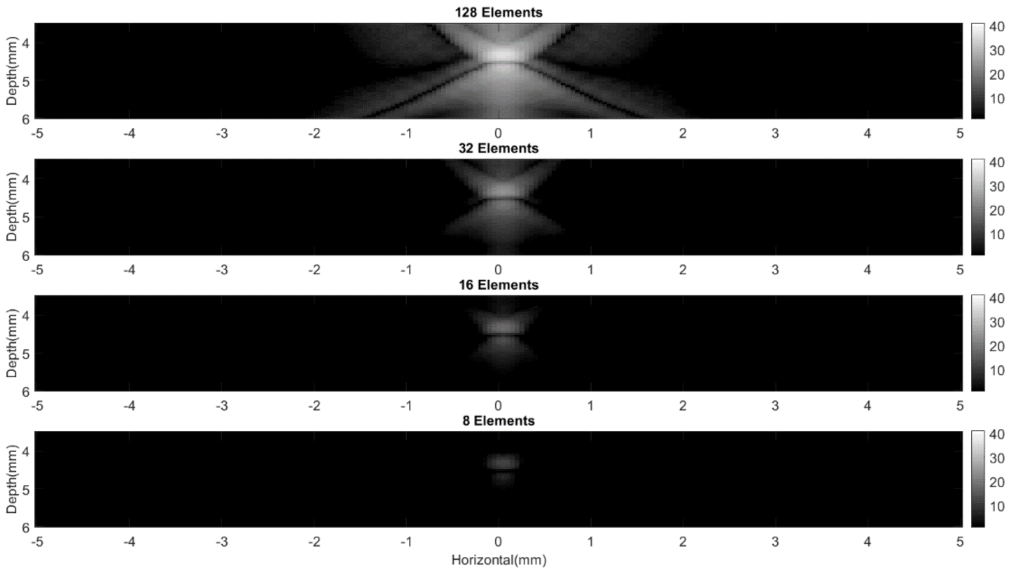

Figure 4.6: Delay-and-Sum Beamformed Images of one absorber, imaged with (from top to bottom) 128, 32, 16 and 8 elements. The same measurement data is used in all images.

To emphasize the effect of grating lobes, 30 dB is added to the images in Figure 4.6 to shift the baseline. These can be seen in Figure 4.7. As expected, grating lobes appear on images with 32, 16, and 8 channels. The grating lobes are shown in red squares in Figure 4.7. Even though they are not visible in Figure 4.6, grating lobes can sum coherently and reduce resolution and contrast [53].

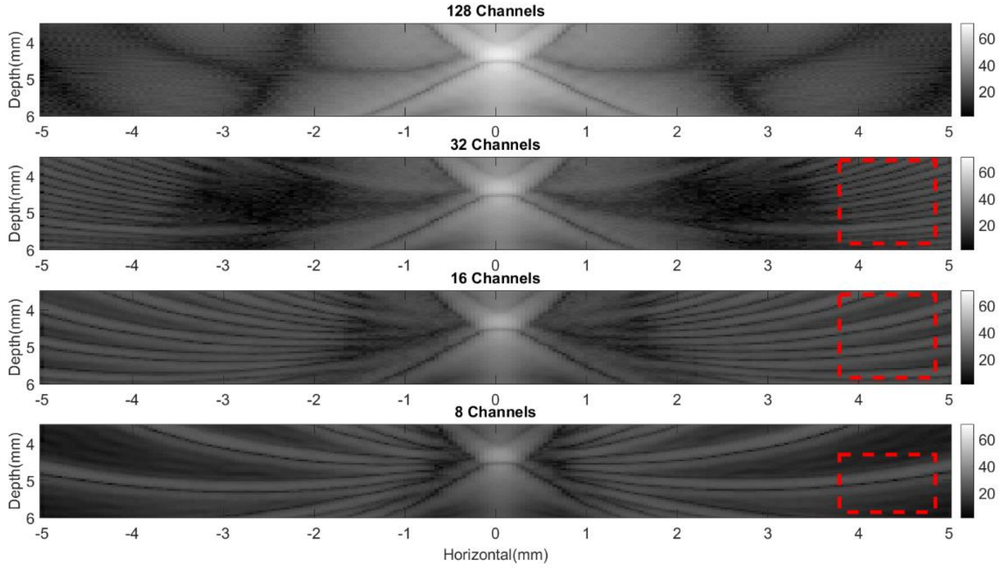

Figure 4.7: 30dB added to images on Figure 4.6 to better visualize grating lobes. The grating lobes are highlighted in the dashed boxes.

CS is applied to the same data, which can be seen in Figure 4.8. In these images, α is set to 0.3 and 100 dB is added. Grating lobes are not observed when CS is applied.

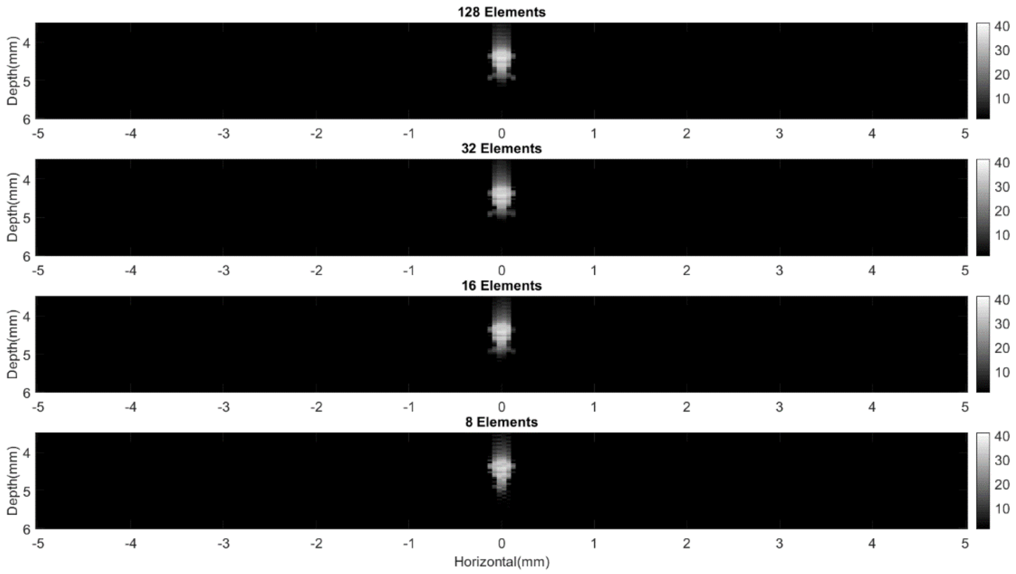

Figure 4.8: CS applied images of one absorber, imaged with (from top to bottom) 128, 32, 16 and 8 elements

CS-based method handles spatially undersampled data better than DAS beamforming, as no grating lobes are present in any of the images. A comparison of lateral profiles of images at $z = 4.5$ mm is shown in Figure 4.9. The profiles in Figure 4.9 summarize how DAS and CS respond to spatial undersampling. The baselines are around the same level (-10 dB) in Figure 4.9(a), but the peak signal power and sidelobes drop as fewer channels are used. There is a 6 dB decrease as the number of channels is halved in Figure 4.9(a), which was expected. In Figure 4.9(b), the highest level remains the same, and there are no sidelobes. Undersampling doesn't affect lateral resolution in both images. Lateral resolutions are 150 μm for CS images and 530 μm for DAS beamformed images, so CS reconstruction results in a narrower FWHM.

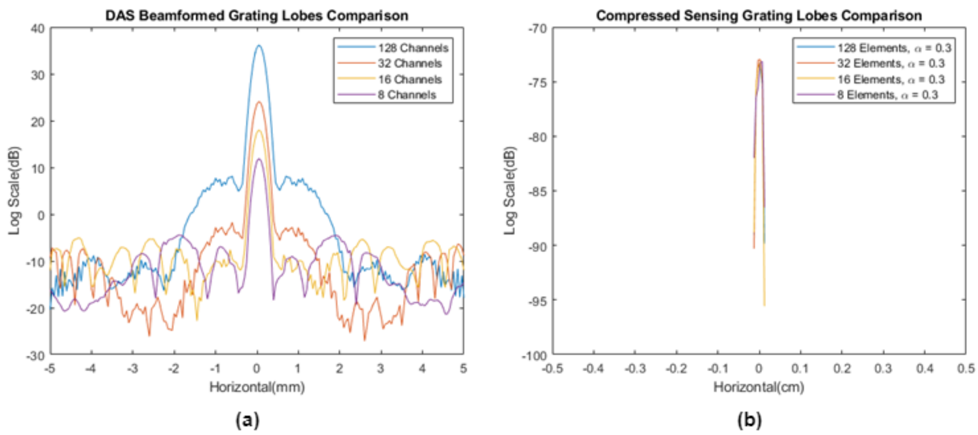

Figure 4.9: Comparison of Horizontal Profiles of a Point Absorber (with 0.1 mm diameter) for (a) DAS Beamforming and (b) Compressed Sensing

Table 4.3. Contrast Comparison of DAS and CS vs Number of Elements Used in Reception

Number of Elements Used	DAS CR	CS CR
128	42.11 dB	35.15 dB
32	43.85 dB	33.04 dB
16	28.99 dB	32.57 dB
8	17.02 dB	31.15 dB

The contrast calculated in the images is given in Table 4.3. Even though DAS contrast is higher than CS contrast for 128 and 32 elements, CS outperforms DAS as fewer elements are used. When fewer elements are used in beamforming algorithm, the maximum pixel intensity decreases. This causes a loss of image contrast. CS contrast is less affected by a change in the number of elements used, there is only a 4 dB decrease in contrast when $1/16^{th}$ of the elements is used.

4.3 Two-Point Resolution

Two-point resolution test takes both the sidelobes and grating lobes into account. Sidelobes might cause close objects to blur together in the images by overlapping in the DAS beamforming process. Spatial undersampling introduces grating lobes that might overlap with the targets. In that case, the targets could be undetectable even without sidelobes overlapping.

We image two targets (0.1 mm diameter) placed at the same depth with differing spacing at 4.5 mm. Spacings are 1 mm, 0.8 mm, 0.4 mm, and 0.2 mm.

The imaging grid spans $x = -1.6$ mm to $x = 1.6$ mm horizontally with 64 pixels and $z = 3$ mm to $z = 6$ mm laterally with 60 pixels. The imaging grid and the geometry of simulation is shown in Figure 4.10. We used a 32-element transducer with a 0.4 mm pitch. The transducer has $f_c = 2.75$ MHz center frequency and $bw = 160\%$ fractional bandwidth. The spectra of the recorded signals are once again in 500 kHz and 5 MHz range. The highest frequency content of PA waves is at 5 MHz, so $\lambda = 290$ µm. We used a sampling frequency of $f_s = 80$ MHz. In CS images α is taken as 0.125 and 95 dB is added for all images.

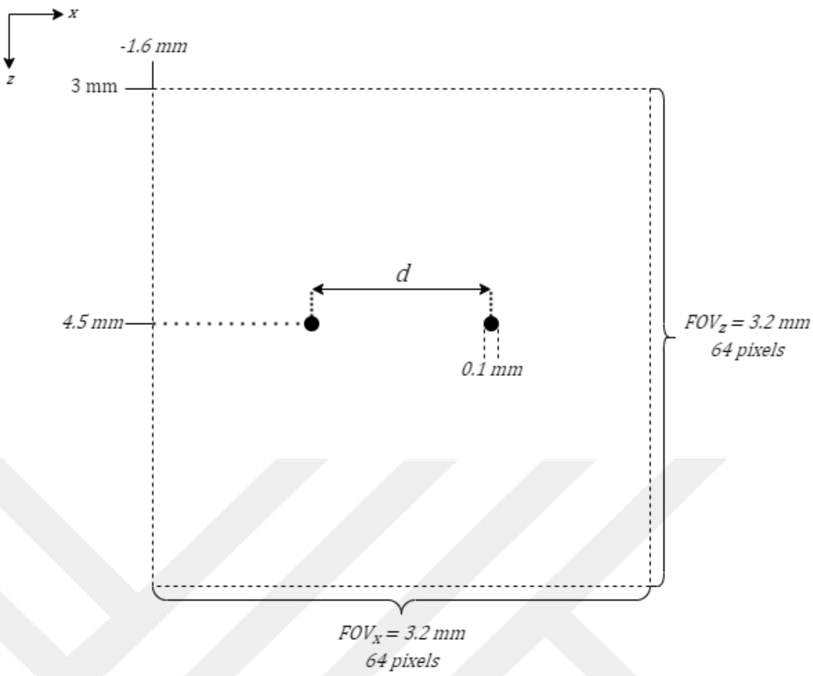

Figure 4.10. Simulation geometry and imaging grid for two-point test. Two absorbers with 0.1 mm diameters are placed at 4.5 mm depth. Four different d (the spacing between two absorbers) are used in simulations. The spacing is kept at 1 mm, 0.8 mm, 0.4 mm, and 0.2 mm in the simulations. The imaging grid spans 3.2 mm in both axial and lateral directions with 64 pixels on each side.

The reconstructed images are shown in Figure 4.11. Images on the left column are reconstructed using the CS-based method. DAS beamforming is applied to the images on the right column. DAS beamformed images, Figures 4.11(b,d,f,g), display wider mainlobes. For 1 mm and 0.8 mm separations, Figures 4.11(a-d), both the CS-based method and the DAS beamforming can identify the two targets. For 0.4 mm separation, which corresponds to 1.4λ, mainlobes in the DAS beamformed image overlap, and two objects blend visually. CS image for 0.4 mm seperation, Figure 4.11(e), is able to distinguish the two targets at this separation. For 0.2 mm separation (0.7λ), the two objects are indistinguishable using both methods.

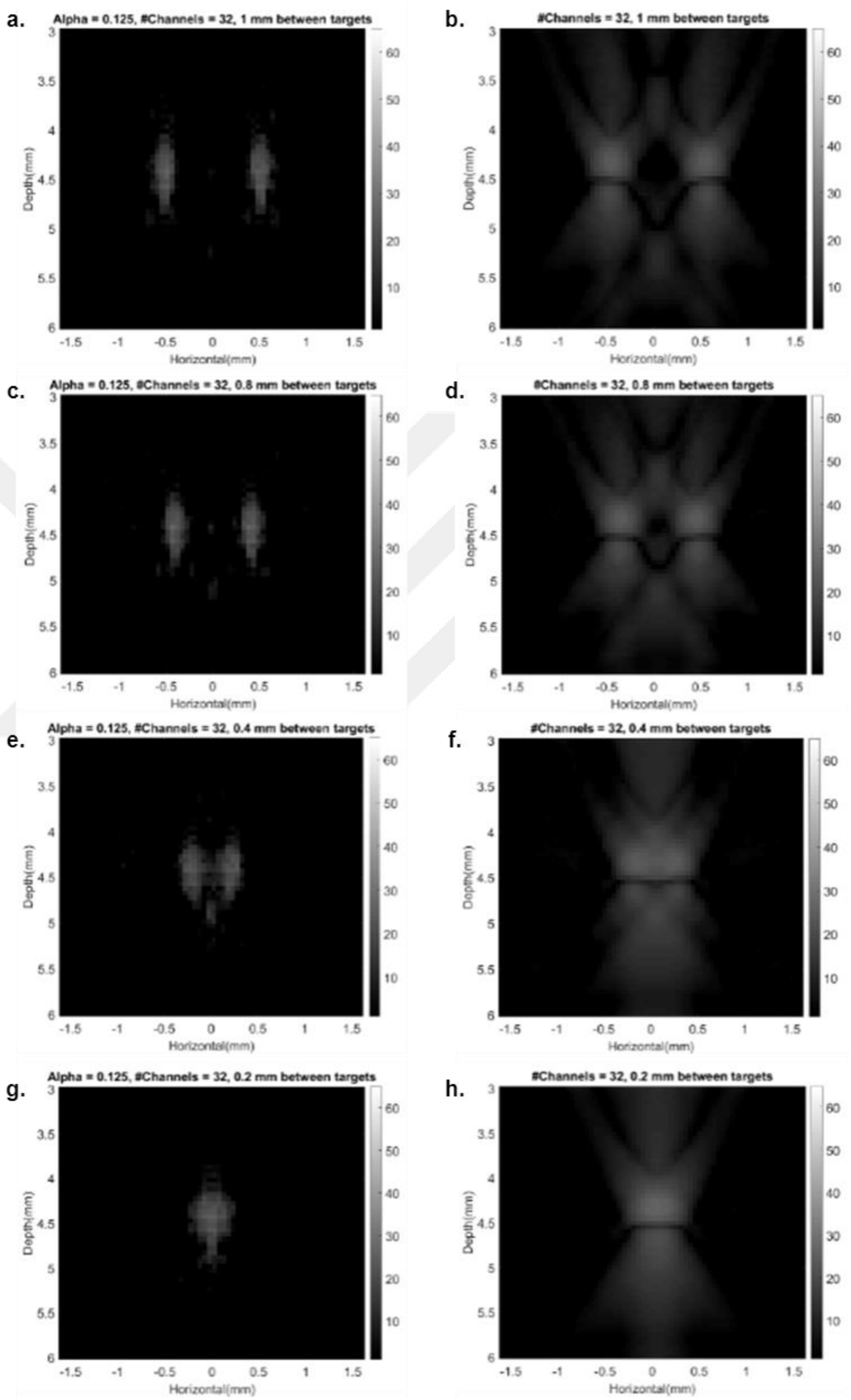

Figure 4.11: Two-point Resolution Comparisons. CS and DAS images for (a)-(b): 1 mm spacing, (c)-(d): 0.8 mm spacing, (e)-(f): 0.4 mm spacing, (g)-(h): 0.2 mm spacing, respectively. All targets have 0.1 mm diameter.

For further inspection, we plot the lateral profiles of images at $z = 4.5$ mm depth in Figure 4.12. For 0.8 mm spacing, Figure 4.12(b), overlapping of targets starts in DAS images. For 0.4 mm spacing, Figure 4.12(c), DAS is unable to distinguish two targets as there isn't a -6 dB drop in the separation. In both images, CS can clearly distinguish two targets. For 0.2 mm separation, Figure 4.12(d), neither reconstruction method can detect two targets.

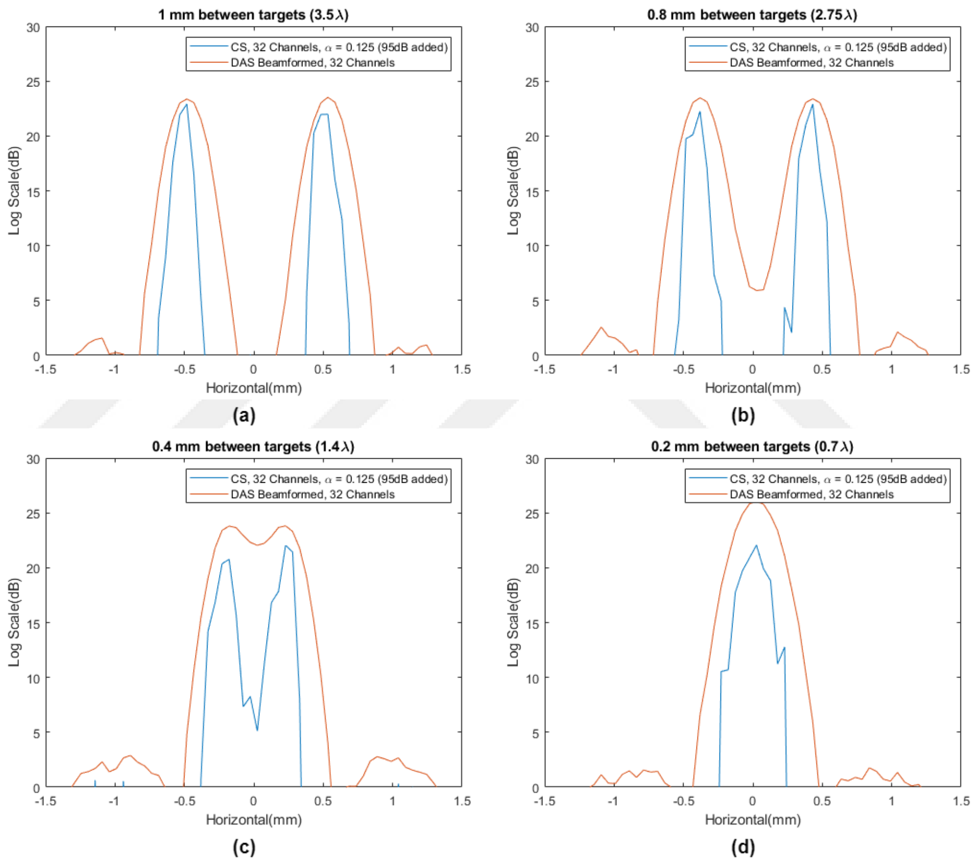

Figure 4.12: Comparison of Lateral Profiles of the Images in Figure 4.11 at targets' depth ($z = 4.5$ mm)

Overall, CS results in a finer resolution and can suppress grating lobes, as shown in the previous two subsections. As a combination of the two, CS performs better at detecting targets close to each other.

Chapter 5

Experimental Results

We conducted experiments to test the performance of CS-based reconstruction method with DAS beamforming. The experiments also allow us to analyze how the model handles noise. In our experiments, the phantom is imaged using optical pulses with different wavelengths and pulse energies given in Table 5.1. In addition, noise measurements of the optoacoustic phantom are taken. The measurement setup is given in detail in Section 2.1. In both CS reconstruction and DAS beamforming, we used only 32 equally spaced elements of the 128-element phased array that spans the entire aperture.

Table 5.1. Wavelength and Energy of the Laser Pulses Used

Wavelength	670 nm	680 nm	750 nm	780 nm	820 nm
Energy Level #1	8.0 mJ	8.3 mJ	4.5 mJ	4.1 mJ	3.5 mJ
Energy Level #2	5.9 mJ	6.0 mJ	3.3 mJ	3.0 mJ	2.66 mJ
Energy Level #3	3.0 mJ	3.1 mJ	1.8 mJ	2.1 mJ	1.45 mJ
Energy Level #4	2.2 mJ	2.4 mJ	1.4 mJ	1.3 mJ	1.15 mJ

ICG has a nonlinear response to optical illumination. For 0.5 mM ICG concentration, optical absorption is highest when pulses around 800 nm wavelength are used [75].

We define the center of our transducer as the origin of our coordinate axes. The imaging grid is located between $x = -3.2$ mm and $x = 3.2$ mm laterally, $z = 18$ mm and $z = 24.4$ mm vertically, with 128 pixels on each side. The pixel resolution is 50 μm on either side. The target and the imaging grid are illustrated on Figure 5.1. 80 dB gain is added to all CS images. The choice of the relaxation constant α is made heuristically and separately for each wavelength and energy combination.

In the experiments the phased array transducer used has a center frequency of $f_c = 7.5$ MHz and a fractional bandwidth of $bw = 70\%$.

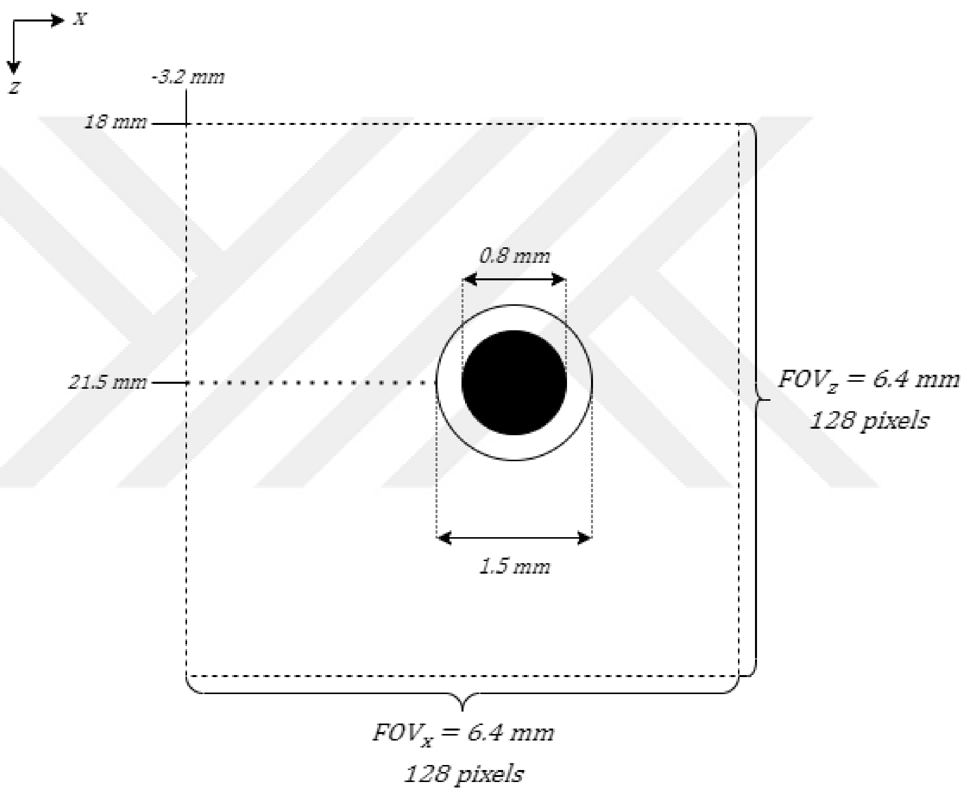

Figure 5.1. Illustration of the target and imaging grid. The target is a polymer tube filled with 0.5 mM ICG. The target is placed at 21.5 mm depth. The outer and inner diameters of the tube are 1.5 mm and 0.8 mm, respectively. The thickness of the tube is 0.35 mm. The imaging grid spans 6.4 mm in both axial and lateral resolutions with 128 pixels on either side.

5.1 Choice of Relaxation Factor (α) in Presence of Noise

In the presence of noise, the choice of α is a crucial factor in the quality of the images. A proper selection of α can alleviate the effects of poor SNR in the measurement data. Figure 5.2 shows the effect α on the CS images. The DAS beamformed image is shown in Figure 5.2(a). Figure 5.2(b-d) shows the CS-based reconstruction algorithm for different α values. The images are all reconstructed from the same measurements. Optical pulses with 670 nm wavelength and 8.0 mJ pulse energy are used.

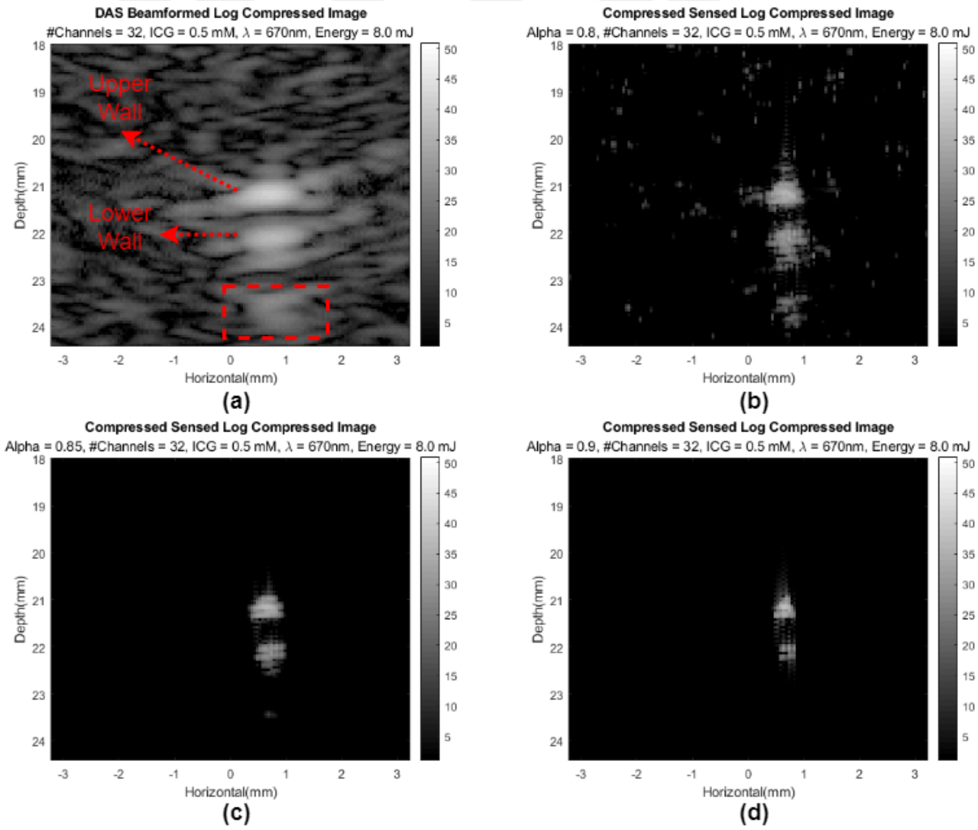

Figure 5.2: Four Images Reconstructed from the Same Measurement. (a) DAS Beamformed Image, (b) CS Image for $\alpha = 0.8$, (c) CS Image for $\alpha = 0.85$, (d) CS Image for $\alpha = 0.9$. The target in the measurements is a polymer tube with an outer diameter of 1.5 mm and inner diameter of 0.8 mm, filled with ICG. The

upper and lower walls of the target are shown in (a) with dotted lines and their reflection is shown in the dashed rectangle.

The lower and upper walls of the polymer tube are detected as shown in the images. These are marked for convenience on Figure 5.2(a). The reflected PA waves inside the tube manifest itself as another reflected spot. This is also shown in Figure 5.2(a) in dashed rectangle. Depending on the choice of α, this reflection can also be seen when CS is used. It is visible in Figure 5.2(b) but not in 5.2(c, d).

When the choice of α is low the algorithm is forced to incorporate the additive noise and the reflected PA waves into the recovery process. This results in speckles and the reflection, as seen in Figure 5.2(b). As α increases, Figure 5.2(c), the speckles disappear, and the reflection becomes less observable. When α is increased further in Figure 5.2(d), crucial information is disregarded, and the target cannot be entirely detected. Among these images, $\alpha = 0.85$ results in the best image quality as it is artifact-free, and the target is fully detected.

5.2 Compressed Sensed Images vs. Wavelength and Pulse Energy

Images from measurements are reconstructed using DAS beamforming and CS-based algorithm. Figures 5.3-5.7 are grouped based on the wavelengths of the optical pulse used. In these figures, each row of images corresponds to a specific energy level. On each row, SNR as a function of depth, the DAS beamformed image and CS image with an appropriate α are given.

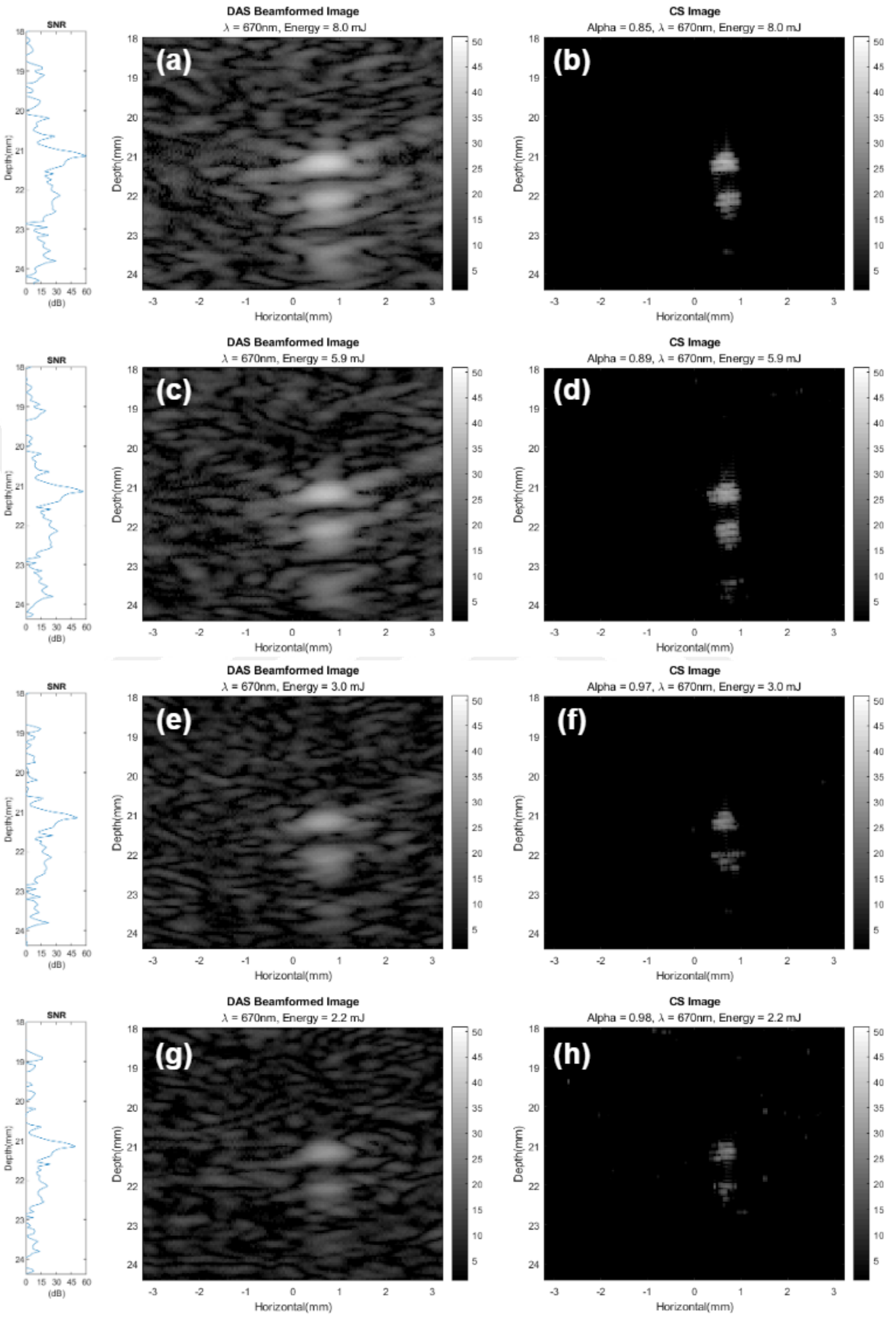

Figure 5.3: Images Reconstructed Using Laser Light with 670 nm. From top to bottom, the pulse energies are 8.0 mJ, 5.9 mJ, 3.0 mJ and 2.2 mJ respectively. While applying CS, α are chosen as 0.85, 0.89, 0.97 and 0.98 respectively. On each row SNR as a function of depth for the corresponding energy level is plotted. The target polymer tube has 1.5 mm outer and 0.8 mm inner diameters.

Figure 5.3 shows the images obtained with DAS and CS method for a fixed pulse wavelength and different pulse energies. As the optical pulse energy decreases, SNR decreases as well. For lower energy levels, ICG produces a weaker response as well. This effect can be observed by the peak pixel intensities of the beamformed images, Figures 5.3(a, c, e, g). A similar effect is also observable in CS images, Figures 5.3(b, d, f, h). However, CS offers improved speckle reduction compared to DAS images. The upper and lower walls of the tube are more observable in CS images.

In Table 5.2, the highest SNR value obtained from DAS images, the peak pixel intensity in all images, and image contrasts measured in the images are given for different pulse energies.

Table 5.2. Comparison of peak SNR in DAS images, peak pixel intensity in DAS and CS images, contrast ratio (CR) in DAS and CS images versus the pulse's energy. The wavelength of the optical pulses is 670 nm.

Pulse Energy	SNR	DAS Peak Intensity	DAS CR	CS Peak Intensity	CS CR
8.0 mJ	60.16 dB	41.97 dB	29.78 dB	36.74 dB	44.73 dB
5.9 mJ	57.22 dB	39.01 dB	34.41 dB	32.66 dB	42.17 dB
3.0 mJ	51.26 dB	33.08 dB	20.79 dB	26.89 dB	41.73 dB
2.2 mJ	49.28 dB	30.67 dB	24.71 dB	26.63 dB	37.48 dB

In CS images, the contrast is higher than in DAS images, and it increases as higher pulse energy is used. The axial and lateral FWHM resolutions of the upper wall of the tube (located at 21 mm depth) are given in Table 5.3. CS results in a narrower FWHM in both lateral and axial directions. The difference is more noticeable in the lateral direction. For 8.0 mJ, 5.9 mJ, and 3.0 mJ, both DAS and CS can adequately resolve the thickness of the polymer tube (which is 350 μm). However, when 2.2 mJ is used, the target becomes visually less observable in Figures 5.3(g, h).

Table 5.3. Comparison of FWHM of DAS and CS in lateral and axial directions versus optical pulse energy. The FWHMs are taken from the part of the tube located at 21 mm depth.

Pulse Energy	DAS FWHM (Lateral)	CS FWHM (Lateral)	DAS FWHM (Axial)	CS FWHM (Axial)
8.0 mJ	795 µm	397 µm	305 µm	276 µm
5.9 mJ	770 µm	353 µm	360 µm	293 µm
3.0 mJ	820 µm	355 µm	390 µm	350 µm
2.2 mJ	770 µm	335 µm	353 µm	140 µm

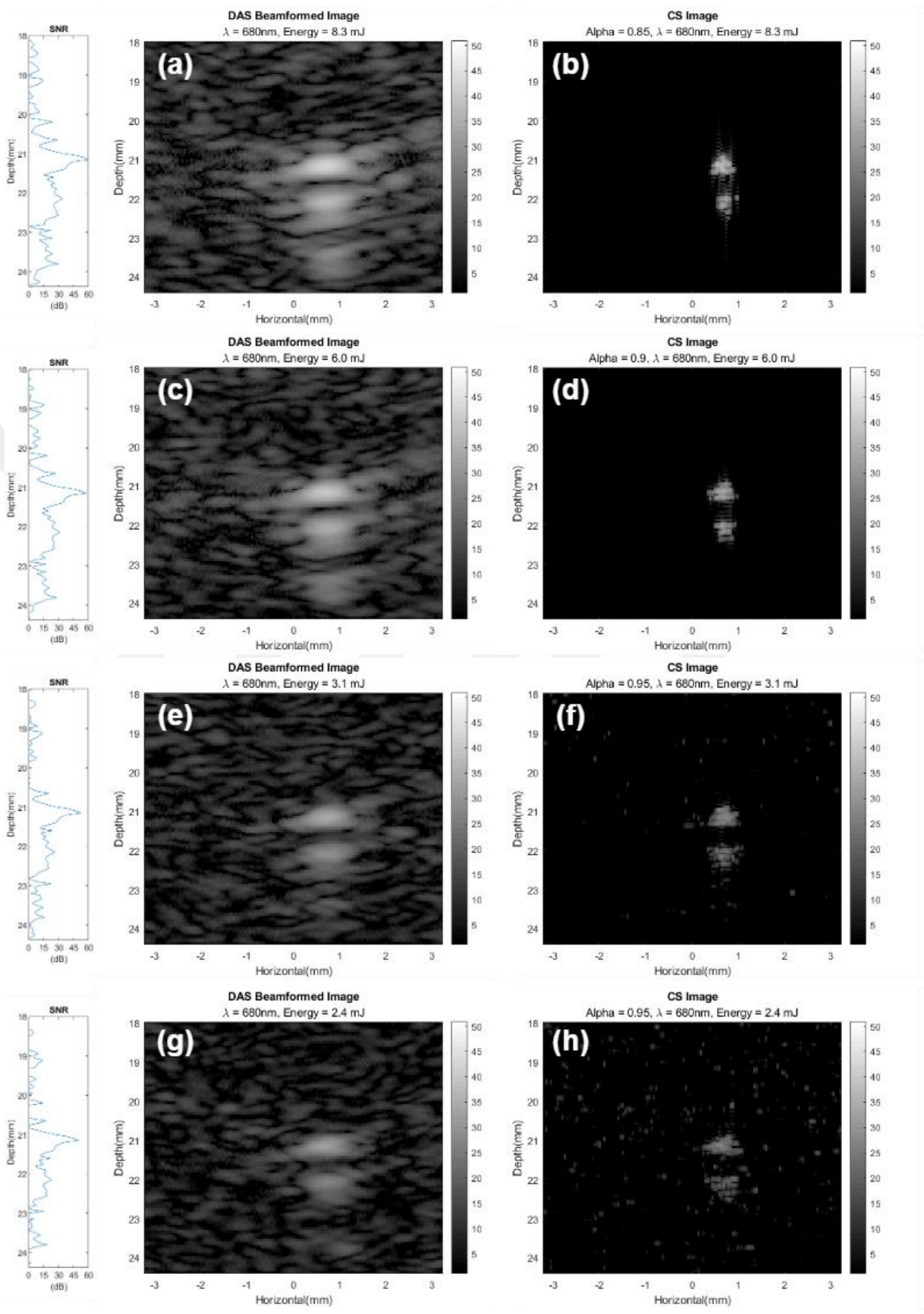

Figure 5.4: Images Reconstructed Using Laser Light with 680 nm. From top to bottom, the pulse energies are 8.3 mJ, 6.0 mJ, 3.1 mJ and 2.4 mJ respectively. While applying CS, α are chosen as 0.85, 0.90, 0.95 and 0.95 respectively. On each row SNR as a function of depth for the corresponding energy level is plotted. The target polymer tube has 1.5 mm outer and 0.8 mm inner diameters.

In Figure 5.4, an optical pulse with 680 nm wavelength is used. The SNR, peak pixel intensity in DAS and CS, and contrast in the reconstructed images are given in Table 5.4.

Table 5.4. Comparison of peak SNR in DAS images, peak pixel intensity in DAS and CS images, contrast ratio (CR) in DAS and CS images versus the pulse's energy. The wavelength of the optical pulses is 680 nm.

Pulse Energy	SNR	DAS Peak Intensity	DAS CR	CS Peak Intensity	CS CR
8.3 mJ	60.61 dB	42.22 dB	33.86 dB	38.00 dB	42.89 dB
6.0 mJ	58.01 dB	39.61 dB	30.78 dB	34.66 dB	43.22 dB
3.1 mJ	52.59 dB	34.00 dB	24.55 dB	27.73 dB	36.84 dB
2.4 mJ	50.57 dB	32.33 dB	23.97 dB	27.26 dB	34.46 dB

The results are similar to the ones in Figure 5.3. Both DAS and CS methods lose image contrast and peak intensity as SNR decreases. Speckles are present in all DAS beamformed images, Figures 5.4(a, c, e, g), whereas they can only be seen for lower SNR values in CS images, Figures 5.4(f, g). Speckles are more severe in Figure 5.4(g), but it is still an improvement from DAS images.

The resolutions are compared in Table 5.5. The FWHMs are calculated on the upper wall of the tube. The lateral resolution does not change for both DAS and CS methods when the pulse energies are high, approximately 770 μm and 350 μm, respectively. CS method and DAS beamforming perform similarly in terms of axial resolution.

Table 5.5. Comparison of FWHM of DAS and CS in lateral and axial directions versus optical pulse energy. The FWHM are measured from the part of the tube located at 21 mm depth.

Pulse Energy	DAS FWHM (Lateral)	CS FWHM (Lateral)	DAS FWHM (Axial)	CS FWHM (Axial)
8.3 mJ	778 µm	324 µm	390 µm	403 µm
6.0 mJ	793 µm	345 µm	390 µm	282 µm
3.1 mJ	750 µm	386 µm	285 µm	445 µm
2.4 mJ	680 µm	486 µm	245 µm	206 µm

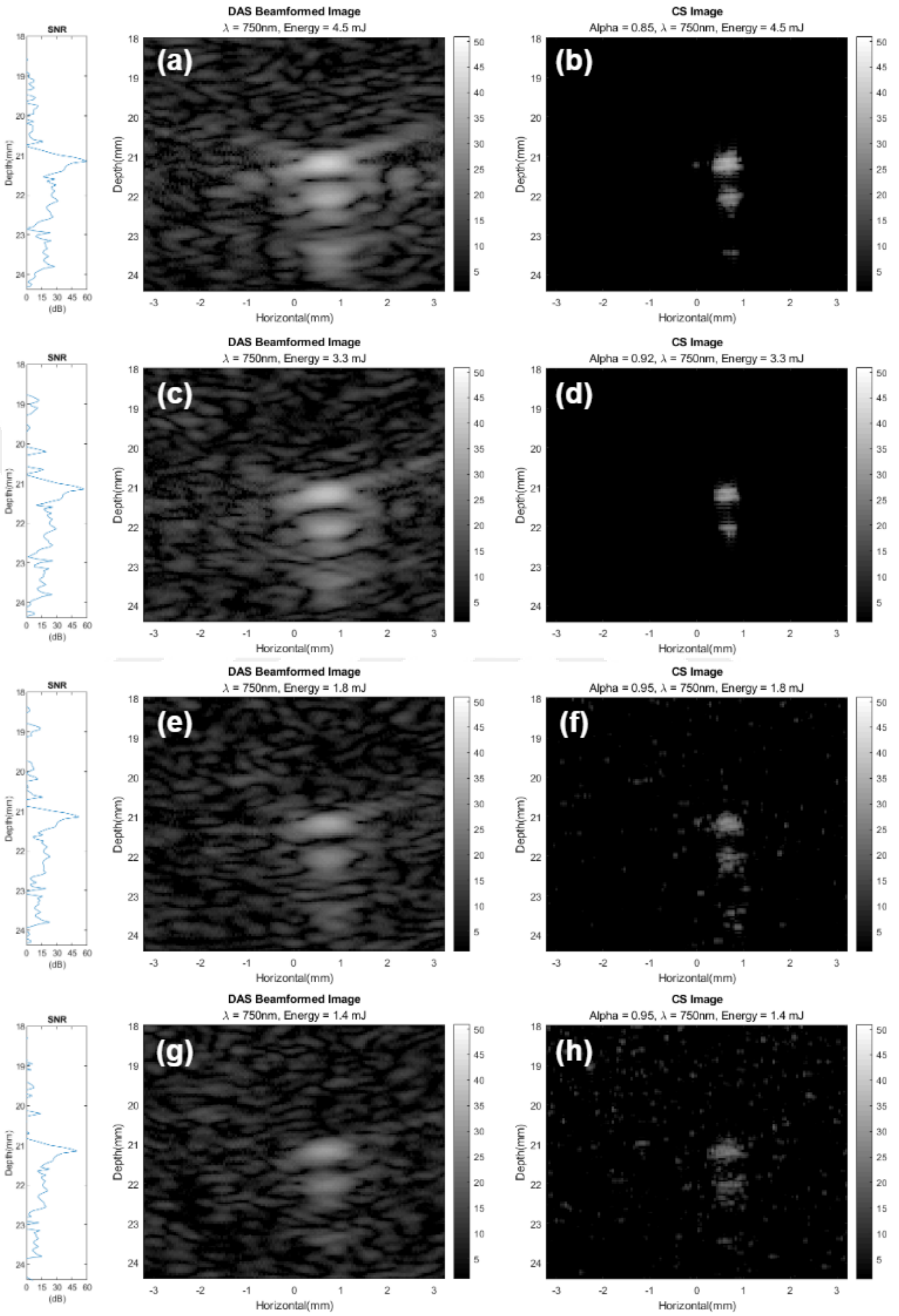

Figure 5.5: Images Reconstructed Using Laser Light with 750 nm. From top to bottom, the pulse energies are 4.5 mJ, 3.3 mJ, 1.8 mJ and 1.4 mJ respectively. While applying CS, α are chosen as 0.85, 0.82, 0.95 and 0.95 respectively. On each row SNR as a function of depth for the corresponding energy level is plotted. The target polymer tube has 1.5 mm outer and 0.8 mm inner diameters.

An optical pulse with a 750 nm wavelength is used in Figure 5.5. For this wavelength, the maximum pulse energy is almost half of what we could produce at 670 nm and 680 nm. We can better understand how the choice of α effects reconstruction in Figure 5.5(d, f, g). The lower wall of the tube shrinks from Figure 5.5(b) to Figure 5.5(d, f, g). In Figure 5.5(f, g), we tried to keep a low α, so that both the upper and lower part of the polymer tube can be visible in the images, but the speckles could not be reduced.

Table 5.6 shows the SNR, Peak pixel intensities for DAS and CS, and contrast for DAS and CS. In Figure 5.5(a), even though the optical pulse energy is half of the ones in Figure 5.3(a) and Figure 5.4(a), the peak SNR remains the same. This is caused by the nonlinear absorption property of ICG. It is more absorbing in the 750-800 nm region, so we are not affected by low energy levels as much. Lastly, CS has a better resolution lateral direction.

Table 5.6. Comparison of peak SNR in DAS images, peak pixel intensity in DAS and CS images, contrast in DAS and CS images versus the pulse's energy. The wavelength of the optical pulses is 750 nm.

Pulse Energy	SNR	DAS Peak Intensity	CS Peak Intensity	DAS Contrast	CS Contrast
4.5 mJ	59.80 dB	41.78 dB	36.14 dB	34.68 dB	48.39 dB
3.3 mJ	57.07 dB	38.91 dB	32.41 dB	32.45 dB	46.07 dB
1.8 mJ	52.13 dB	33.84 dB	28.07 dB	29.85 dB	38.22 dB
1.4 mJ	50.05 dB	32.12 dB	24.62 dB	24.72 dB	34.51 dB

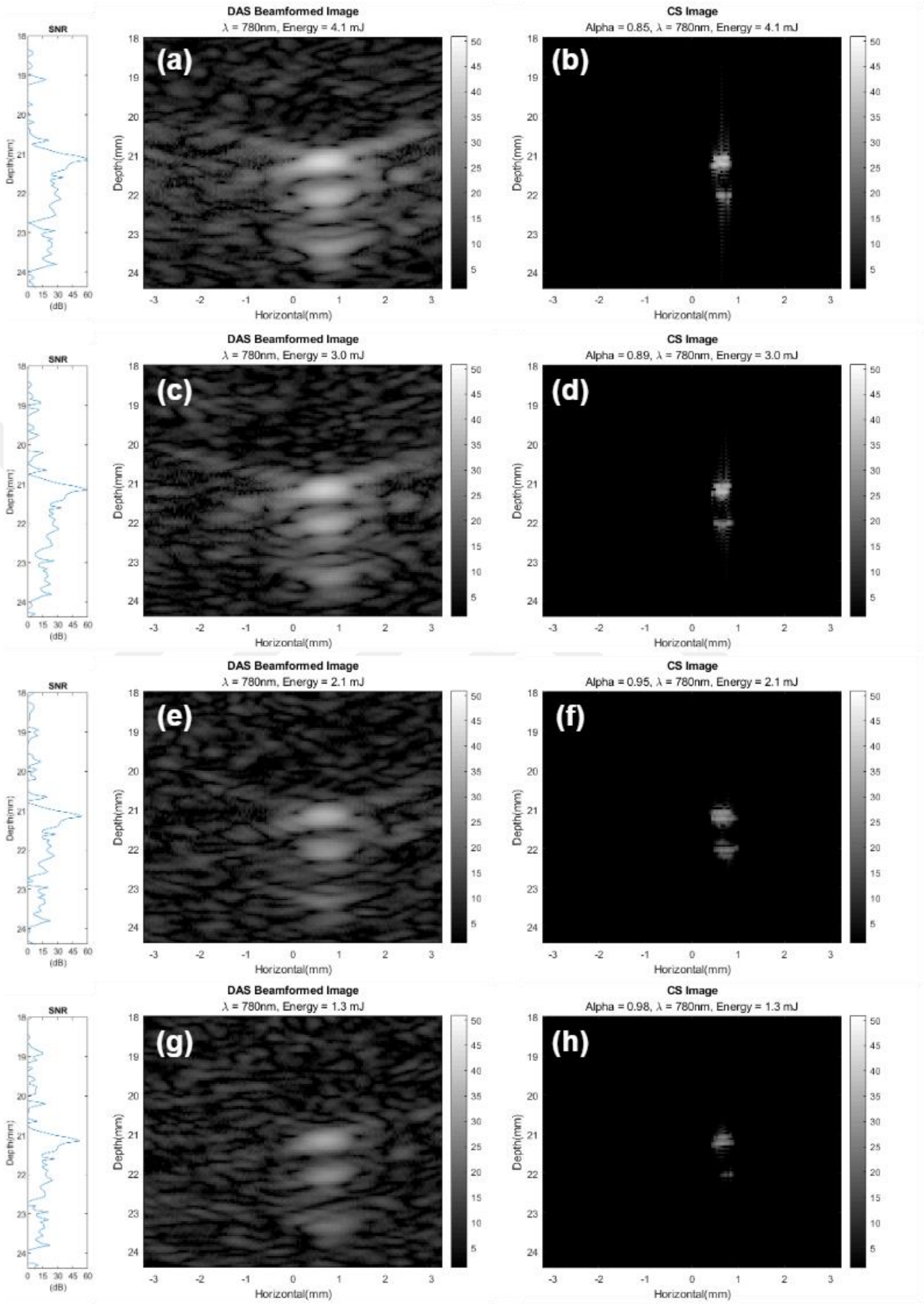

Figure 5.6: Images Reconstructed Using Laser Light with 780 nm. From top to bottom, the pulse energies are 4.1 mJ, 3.0 mJ, 2.1 mJ and 1.3 mJ respectively. While applying CS, α are chosen as 0.85, 0.89, 0.95 and 0.98 respectively. On each row SNR as a function of depth for the corresponding energy level is plotted. The target polymer tube has 1.5 mm outer and 0.8 mm inner diameters.

We further performed measurements with 780 nm and 820 nm, the results of which are shown in Figures 5.6 and 5.7. In these images, the lower wall is not as well detected in CS method when compared to DAS beamforming. This is because the lowest pulse energies used in this study are obtained at 780 nm and 820 nm wavelengths, which causes low SNR. As a result, the lower wall of the polymer tube is harder to detect in these images. This detection problem is visually observable particularly in 5.6(h) and 5.7(f, h). In Figures 5.6 and 5.7, CS performs better in terms of lateral resolution and contrast.

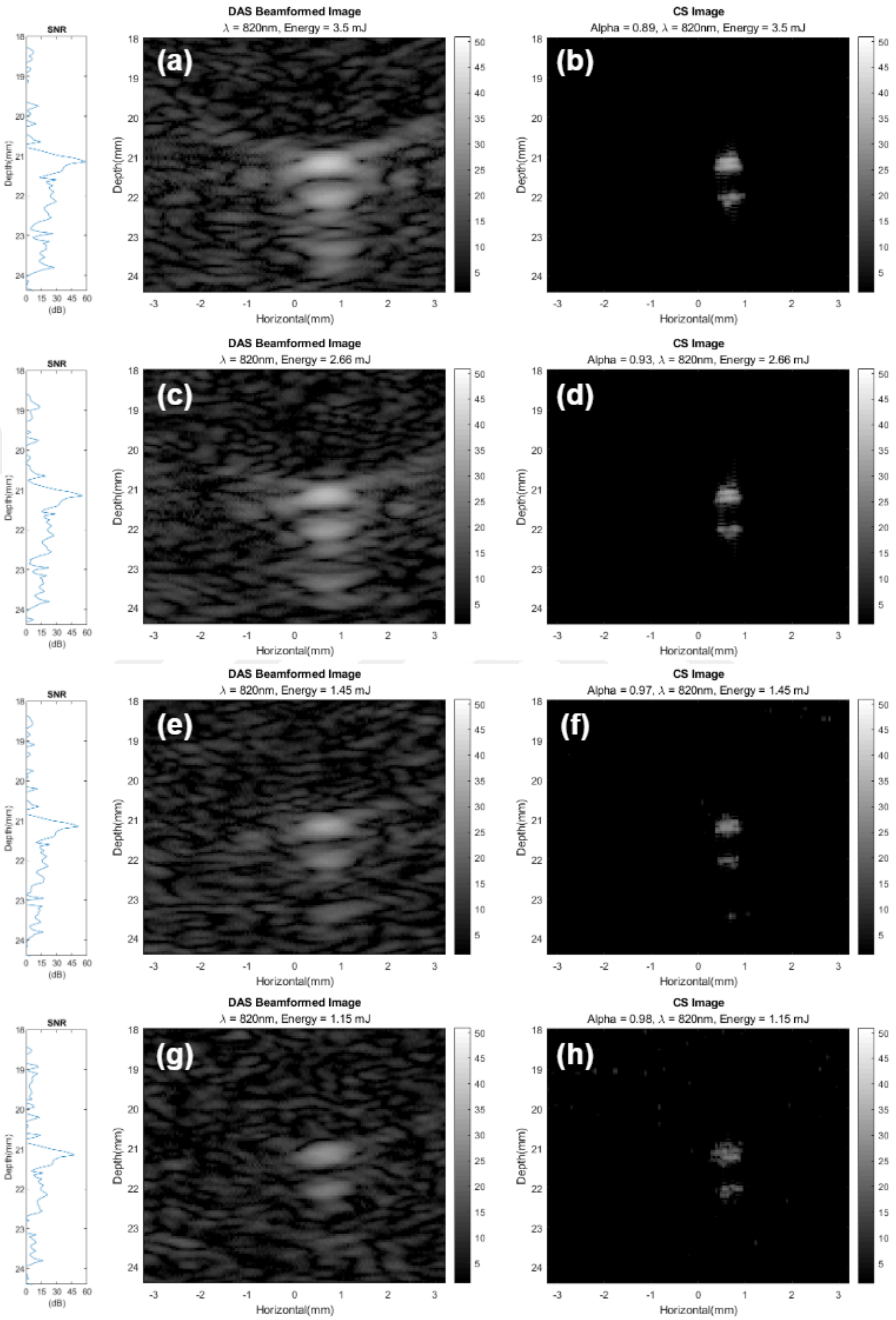

Figure 5.7: Images Reconstructed Using Laser Light with 820 nm. From top to bottom, the pulse energies are 3.5 mJ, 2.66 mJ, 1.45 mJ and 1.15 mJ respectively. While applying CS, α are chosen as 0.89, 0.93, 0.97 and 0.98 respectively. On each row SNR as a function of depth for the corresponding energy level is plotted. The target polymer tube has 1.5 mm outer and 0.8 mm inner diameters.

For each pulse wavelength, the decrease in pulse energy results in a lower SNR. Both DAS and CS are negatively affected by low SNR as peak pixel intensity and image contrast decrease. For lower energy values, CS images cannot completely suppress the speckles, but it still performs better than DAS beamformed images in that regard.

In the experiments, the CS-based method always produces images with better lateral FWHM. Lateral FWHM of the upper wall of the tube is measured as approximately 350 µm in all CS images and 750 µm in all DAS images. For the lowest SNR levels, CS cannot fully resolve the lower wall of the polymer tube, as seen in Figures 5.6 and 5.7.

In CS images, regardless of the SNR in the measurement, contrast is better than in DAS beamformed images. Applying CS improves Contrast Ratio by 10.81 dB on average when compared to DAS beamformed images. At high SNR levels, CS can completely resolve the targets and suppress the speckles. As discussed in Section 5.1, the relaxation factor must be close to 1 for low SNR to compensate for the noise.

Lastly, we inspect the behavior of DAS and CS when optical pulses with different wavelengths and similar pulse energies are used. In Figure 5.8, plots of SNR as a function of depth, and axial profiles of CS images are given. The energies of the pulses are approximately 3.3 mJ in all measurements.

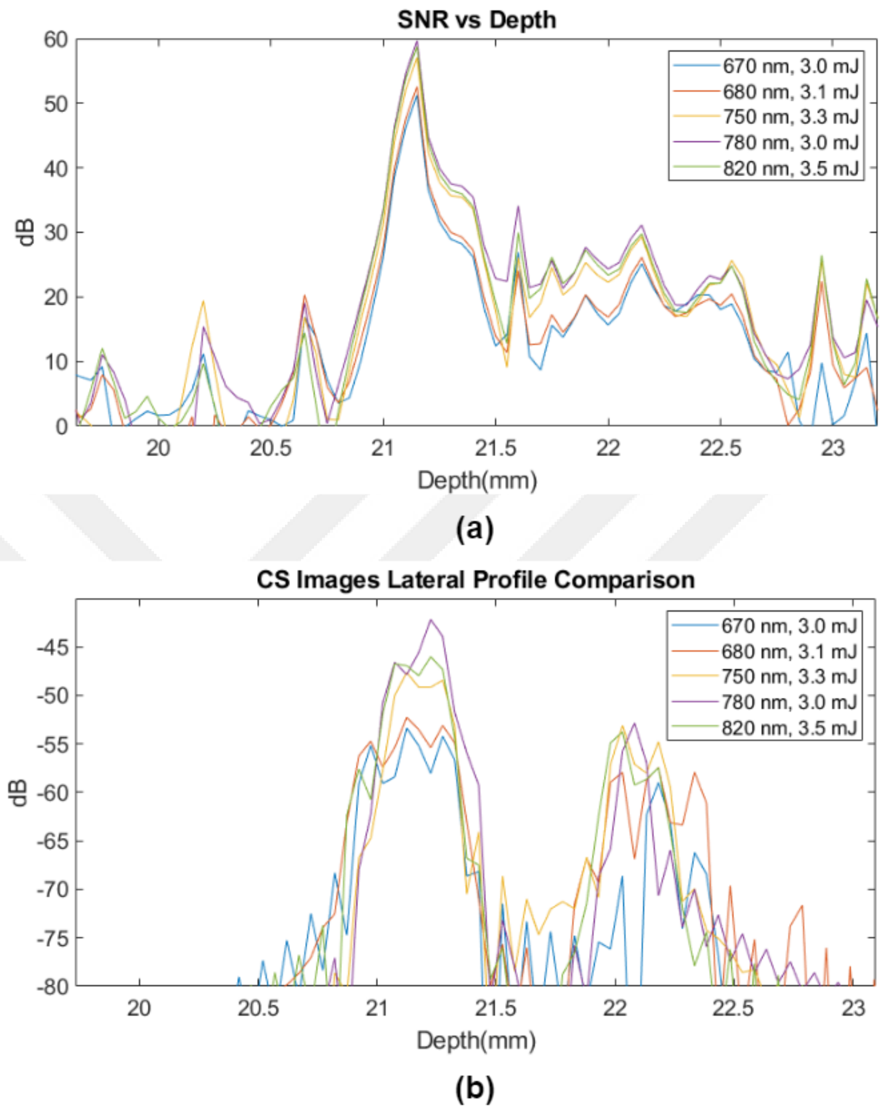

Figure 5.8: SNR and CS Lateral Profile Comparison for Measurements with Equal Pulse Energies

Due to the nonlinear absorption property of ICG, the energy of the generated PA signals differs with wavelength of the optical pulses even though the energies of the pulses used are nearly equal. In Figure 5.8(a), ICG is most responsive to laser pulses with optical wavelengths of 780 nm and 820 nm. This property is also preserved in CS images as seen in Figure 5.8(b). Both of these plots, agree with our expectations for ICG’s absorption characteristic.

Chapter 6

Discussion and Conclusion

We used a CS-based image reconstruction algorithm to reduce the effects of spatial undersampling in PAI. We defined a linear model between the measurements recorded by the phased array transducer and the optical absorption distribution of the region of interest. The forward matrix, K, of our model is constructed analytically. We compared the performance of the CS-based reconstruction method with the DAS beamforming.

We applied DAS beamforming and CS-based image reconstruction method on simulated data. Images with CS have improved quality as they have a narrower FWHM resolution (both axially and laterally) and better image contrast. The depth dependent lateral FWHM is improved the most; up to 0.33 mm reduction in FWHM is observed. For undersampled data, we showed that applying CS does not result in grating lobes. Spatial undersampling results in up to 25 dB loss in contrast in DAS beamformed images. Such a loss is not present in images produced with CS.

Experiments allowed us to assess the CS-based method's performance in the presence of noise. In all CS images, the lateral resolution is improved. CS method reduces the speckles compared to DAS beamforming method for high SNR. In poor SNR conditions, the performance of CS method decreases, and speckles become more prominent. However, it still performs better than DAS beamforming does in that regard. There is an average of 10.4 dB increase in image contrast when CS method is used. CS' improvement of contrast and resolution that was observed in simulations is also confirmed by our experimental results.

In the experiments, we used a single layered optoacoustic phantom with one polymer tube inside. As a future work, targets with varying sizes and optical absorption properties can be used in the experiments and performance of the CS-based algorithm can be inspected. In these experiments, the effects of multilayered medium and different attenuation conditions could also be investigated.

The performance of the CS-based reconstruction depends on the accuracy of the model. To further analyze CS algorithm's performance, the use of other forward models must be investigated. A better model will yield less artifacts and improve the quality of the reconstructed images. We also did not employ any sparsifying transformations in our model. As more complex targets are used, the sparsity requirement of CS might be challenged, so the use of sparsifying transformations and models that fit to these transformations must also be explored.

All the experimental data used in this study can be found in the Bilkent University repository.

Bibliography

[1] P. Beard, "Biomedical Photoacoustic Imaging," *Interface Focus,* vol. 1, no. 4, pp. 602-631, 2011.

[2] A. B. E. Attia, G. Balasundaram, M. Moothanchery, U. S. Dinish, R. Bi, V. Ntziachristos and M. Olivo, "A review of clinical photoacoustic imaging: Current and future trends," *Photoacoustics,* vol. 16, p. 100144, 2019.

[3] M. Xu and L. V. Wang, "Photoacoustic Imaging in Biomedicine," *Review of Scientific Instruments,* vol. 77, no. 4, p. 041101, 2006.

[4] Y. Fan and A. Mandelis, "Development of a laser photothermoacoustic frequency-swept system for subsurface imaging: Theory and experiment," *The Journal of the Acoustical Society of America,* vol. 116, no. 6, pp. 3523-3533, 2004.

[5] K. Maslov, H. F. Zhang, S. Hu and L. V. Wang, "Optical-resolution photoacoustic microscopy for in vivo imaging of single capillaries," *Optics Letters,* vol. 33, no. 9, pp. 929-931, 2008.

[6] G. Langer, K.-D. Bouchal, H. Grün, P. Burgholzer and T. Berer, "Two-photon absorption-induced photoacoustic imaging of Rhodamine B dyed polyethylene spheres using a femtosecond laser," *Optics Express,* vol. 21, no. 19, pp. 22410-22422, 2013.

[7] F. C. P. Masim, H.-L. Liu, M. Porta, T. Yonezawa, A. Balčytis, S. Juodkazis, W.-H. Hsu and K. Hatanaka, "Enhanced photoacoustics from gold nano-colloidal suspensions under femtosecond laser excitation," *Optics Express*, vol. 24, no. 13, pp. 14781-14792, 2016.

[8] L. Li, "Photoacoustic Imaging," *Pathobiology of Human Disease,* pp. 3912-3924, 2014.

[9] S. Zanganeh, H. Li, P. D. Kumavor, U. S. Alqasemi, A. Aguirre, I. Mohammad, C. Stanford, M. B. Smith and Q. Zhu, "Photoacoustic imaging enhanced by indocyanine green-conjugated single-wall carbon nanotubes," *Journal of Biomedical Optics,* vol. 18, no. 9, p. 096006, 2013.

[10] Z. Chaudhary, G. M. Khan, M. M. Abeer, N. Pujara, B. W.-C. Tse, M. A. McGuckin, A. Popat and T. Kumeria, "Efficient photoacoustic imaging using indocyanine green (ICG) loaded functionalized mesoporous silica nanoparticles," *Biomaterials Science,* vol. 7, no. 12, pp. 5002-5015, 2019.

[11] C. Kim, T. N. Erpelding, L. Jankovic and L. V. Wang, "Performance benchmarks of an array-based hand-held photoacoustic probe adapted from a clinical ultrasound system for non-invasive sentinel lymph node imaging," *Philosophical Transactions of the Royal Society of A,* vol. 369, no. 1955, p. 4644–4650, 2011.

[12] J. Xia and L. V. Wang, "Small-animal whole-body photoacoustic tomography: a review," *IEEE Transactions on Biomedical Engineering,* vol. 61, no. 5, pp. 1380-1389, 2014.

[13] M.-L. Li, J. C. Wang, J. A. Schwartz, K. L. Gill-Sharp, G. S. D.V.M. and L. V. Wang, "In-vivo photoacoustic microscopy of nanoshell extravasation from solid tumor vasculature," *Journal of Biomedical Optics,* vol. 14, no. 1, p. 010507, 2009.

[14] V. Tsytsarev, S. Hu, J. Yao, K. I. Maslov, D. Barbour and L. V. Wang, "Photoacoustic microscopy of microvascular responses to cortical electrical stimulation," *Journal of Biomedical Optics*, vol. 16, no. 7, p. 076002, 2011.

[15] M. Li, Y. Tang and J. Yao, "Photoacoustic tomography of blood oxygenation: A mini review," *Photoacoustics*, vol. 10, pp. 65-73, 2018.

[16] T. Agano, N. Sato, H. Nakatsuka, K. Kitagawa, T. Hanaoka, K. Morisono and Y. Shigeta, "Comparative experiments of photoacoustic system using laser light source and LED array light source," in *Proceedings Volume 9323, Photons Plus Ultrasound: Imaging and Sensing 2015*, San Francisco, California, United States, 2015.

[17] B. E. Treeby, "Acoustic attenuation compensation in photoacoustic tomography using time-variant filtering," *Journal of Biomedical Optics,* vol. 18, no. 3, p. 036008, 2013.

[18] J. Yao and L. V. Wang, "Photoacoustic Microscopy," *Laser and Photonics Review,* vol. 7, no. 5, pp. 758-778, 2013.

[19] L. V. Wang and L. Gao, "Photoacoustic Microscopy and Computed Tomography: From Bench to Bedside," *Annual Review of Biomedical Engineering,* vol. 16, pp. 155-185, 2014.

[20] L. V. Wang, "Multiscale photoacoustic microscopy and computed tomography," *Nature Photonics,* vol. 3, pp. 503-509, 2009.

[21] K. Maslov, G. Stoica and L. V. Wang, "In vivo dark-field reflection-mode photoacoustic microscopy," *Optics Letters*, vol. 30, no. 6, pp. 625-627, 2005.

[22] T. Chuangsuwanich, M. Moothanchery, A. T. C. Yan, L. Schmetterer, M. J. A. Girard and M. Pramanik, "Photoacoustic imaging of lamina cribrosa microcapillaries in porcine eyes," *Applied Optics,* vol. 57, no. 17, pp. 4865-4871, 2018.

[23] R. Bi, G. Balasundaram, S. Jeon, H. C. Tay, Y. Pu, X. Li, M. Moothanchery, C. Kim and M. Olivo, "Photoacoustic microscopy for evaluating combretastatin A4 phosphate induced vascular disruption in orthotopic glioma," *Journal of Biophotonics,* vol. 11, no. 10, p. e201700327, 2018.

[24] R. Bi, U. Dinish, C. C. Goh, T. Imai, M. Moothanchery, X. Li, J. Y. Kim, S. Jeon, Y. Pu, C. Kim, L. G. Ng, L. V. Wang and M. Olivo, "In vivo label-free functional photoacoustic monitoring of ischemic reperfusion," *Journal of Biophotonics,* vol. 12, no. 7, p. e201800454, 2019.

[25] M. Moothanchery, R. Bi, J. Y. Kim, S. Jeon, C. Kim and M. Olivo, "Optical resolution photoacoustic microscopy based on multimode fibers," *Biomedical Optics Express,* vol. 9, no. 3, p. 1190–1197, 2018.

[26] V. Periyasamy, N. Das, A. Sharma and M. Pramanik, "1064 nm acoustic resolution photoacoustic microscopy," *Journal of Biophotonics,* vol. 12, no. 5, p. e201800357, 2018.

[27] L. V. Wang and S. Hu, "Photoacoustic Tomography: In Vivo Imaging from Organelles to Organs," *Science,* vol. 335, no. 6075, pp. 1458-1462, 2012.

[28] M. Holotta, C. Kremser, P. Torbica, G. Degenhart, R. Esterhammer, W. Jaschke, H. Grossauer, J. Völkl, R. Nuster and G. Paltauf, "Photoacoustic tomography of ex vivo mouse hearts with myocardial infarction," *Journal of Biomedical Optics,* vol. 16, no. 3, p. 036007, 2011.

[29] M. R. Chatni, J. Xia, K. I. Maslov, Z. Guo, K. Wang, M. A. Anastasio, L. V. Wang, R. Sohn, J. M. Arbeit, Y. Zhang and Y. Xia, "Tumor glucose metabolism imaged in vivo in small animals with whole-body photoacoustic computed tomography," *Journal of Biomedical Optics,* vol. 17, no. 7, p. 076012, 2012.

[30] R. A. Kruger, C. M. Kuzmiak, R. B. Lam, D. R. Reinecke, S. P. D. Rio and D. Steed, "Dedicated 3D photoacoustic breast imaging," *Medical Physics,* vol. 40, no. 13, p. 113301, 2013.

[31] A. Garcia-Uribe, T. N. Erpelding, A. Krumholz, H. Ke, K. Maslov, C. Appleton, J. A. Margenthaler and L. V. Wang, "Dual-Modality Photoacoustic and Ultrasound Imaging System for Noninvasive Sentinel Lymph Node Detection in Patients with Breast Cancer," *Scientific Reports,* vol. 5, p. 15748, 2015.

[32] S. K. Kalva, Z. Z. Hui and M. Pramanik, "Calibrating reconstruction radius in a multi single-element ultrasound-transducer-based photoacoustic computed tomography system," *Journal of the Optical Society of America A,* vol. 35, no. 5, pp. 764-771, 2018.

[33] J. Xia, C. Huang, K. Maslov, M. A. Anastasio and L. V. Wang, "Enhancement of photoacoustic tomography by ultrasonic computed tomography based on optical excitation of elements of a full-ring transducer array," *Optics Letters,* vol. 38, no. 16, pp. 3140-3143, 2013.

[34] J. Xia, M. R. Chatni, K. I. Maslov, Z. Guo, K. Wang, M. A. Anastasio and L. V. Wang, "Whole-body ring-shaped confocal photoacoustic computed tomography of small animals in vivo," *Journal of Biomedical Optics,* vol. 17, no. 5, p. 050506, 2012.

[35] R. A. Kruger, R. B. Lam, D. R. Reinecke, S. P. D. Rio and R. P. Doyle, "Photoacoustic angiography of the breast," *Medical Physics,* vol. 37, no. 11, pp. 6096-6100, 2010.

[36] Y. Wang, Y. Zhan, M. Tiao and J. Xia, "Review of methods to improve the performance of linear array-based photoacoustic tomography," *Journal of Innovative Optical Health Sciences,* vol. 13, no. 2, p. 2030003, 2020.

[37] M. Xu and L. V. Wang, "Universal back-projection algorithm for photoacoustic computed tomography," *Physical Review E,* vol. 71, p. 016706, 2007.

[38] E. Bossy, K. Daoudi, A.-C. Boccara and M. Tanter, "Time reversal of photoacoustic waves," *Applied Physics Letters,* vol. 89, no. 18, p. 184108, 2020.

[39] R. Paridar, M. Mozaffarzadeh, V. Periyasamy, M. Pramanik, M. Mehrmohammadi and M. Orooji, "Sparsity-based beamforming to enhance two-dimensional linear-array photoacoustic tomography," *Ultrasonics,* vol. 96, pp. 55-63, 2019.

[40] G. Matrone, A. S. Savoia, G. Caliano and G. Magenes, "The delay multiply and sum beamforming algorithm in ultrasound B-mode medical imaging," *IEEE Transactions on Medical Imaging,* vol. 34, no. 4, pp. 940-949, 2015.

[41] M. Mozaffarzadeh, A. Mahloojifar, M. Orooji, S. Adabi and M. Nasiriavanaki, "Double-Stage Delay Multiply and Sum Beamforming Algorithm: Application to Linear-Array Photoacoustic Imaging," *IEEE Transactions on Biomedical Engineering,* vol. 65, no. 1, pp. 31-42, 2018.

[42] M. Mozaffarzadeh, A. Mahloojifar, M. Orooji, K. Kratkiewicz, S. Adabi and M. Nasiriavanaki, "Linear-array photoacoustic imaging using minimum variance-based delay multiply and sum adaptive beamforming algorithm," *Journal of Biomedical Optics,* vol. 23, no. 2, p. 026002, 2018.

[43] R. Paridar, M. Mozaffarzadeh, M. Mehrmohammadi and M. Orooji, "Photoacoustic image formation based on sparse regularization of minimum variance beamformer," *Biomedical Optics Express,* vol. 9, no. 6, pp. 2544-2561, 2018.

[44] E. J. Candes and M. B. Wakin, "An Introduction To Compressive Sampling," *IEEE Signal Processing Magazine,* vol. 25, no. 2, pp. 21 - 30, 2008.

[45] J. Provost and F. Lesage, "The Application of Compressed Sensing for Photo-Acoustic Tomography," *IEEE Transactions on Medical Imaging,* vol. 28, no. 4, pp. 585 - 594, 2009.

[46] M. F. Schiffner and G. Schmitz, "Fast pulse-echo ultrasound imaging employing compressive sensing," in *2011 IEEE International Ultrasonics Symposium*, Orlando, FL, USA, 2011.

[47] P. K. Mishra, R. Bharath, P. Rajalakshmi and U. B. Desai, "Compressive sensing ultrasound beamformed imaging in time and frequency domain," in *2015 17th International Conference on E-health Networking, Application & Services (HealthCom)*, Boston, MA, USA, 2015.

[48] G. David, "Time domain compressive beam forming of ultrasound signals," *The Journal of the Acoustical Society of America,* vol. 137, no. 5, p. 10.1121/1.4919302, 2015.

[49] K. J. Francis, P. Mishra, P. Rajalakshmi, S. S. Channappayya and A. Richhariya, "A simple and accurate matrix for model based photoacoustic imaging," in *2016 IEEE 18th International Conference on e-Health Networking, Applications and Services (Healthcom)*, Munich, Germany, 2016.

[50] D. M. Egolf, R. K. W. Chee and R. J. Zemp, "Sparsity-based reconstruction for super-resolved limited-view photoacoustic computed tomography deep in a scattering medium," *Optics Letters,* vol. 43, no. 10, pp. 2221-2224, 2018.

[51] M.-L. Li, Y.-C. Tseng and C.-C. Cheng, "Model-based correction of finite aperture effect in photoacoustic tomography," *Optics Express,* vol. 18, no. 25, pp. 26285-26292, 2010.

[52] C.-H. Chiu, Y. Chuo and M.-L. Li, "Image reconstruction of photoacoustic tomography based on finite-aperture-effect corrected compressed sensing algorithm," in *Proceedings Volume 8943, Photons Plus Ultrasound: Imaging and Sensing 2014*, San Francisco, California, United States, 2014.

[53] C.-H. Chiu and M.-L. Li, "Compressive-sensing like grating-lobe suppressed image reconstruction for photoacoustic linear array imaging," in *IEEE International Ultrasonics Symposium*, Chicago, IL, USA, 2014.

[54] R. Shang, R. Archibald, A. Gelb and G. P. Luke, "Sparsity-based photoacoustic image reconstruction with a linear array transducer and direct measurement of the forward model," *Journal of Biomedical Optics,* vol. 24, no. 3, p. 031015, 2018.

[55] S. Vilov, B. Arnal, E. Hojman, Y. C. Eldar, O. Katz and E. Bossy, "Super-resolution photoacoustic and ultrasound imaging with sparse arrays," *Scientific Reports,* vol. 10, p. 4637, 2020.

[56] Y. Kumru and H. Köymen, "Beam coding with orthogonal complementary Golay codes for signal-to-noise ratio improvement in ultrasound mammography," *The Journal of the Acoustical Society of America,* vol. 144, no. 3, p. 10.1121/1.5068277, 2018.

[57] "k-Wave: A MATLAB toolbox for the time-domain simulation of acoustic wave fields," [Online]. Available: http://www.k-wave.org/documentation/example_us_bmode_linear_transducer.php. [Accessed 31 January 2022].

[58] R. Manwar, M. Zafar and Q. Xu, "Signal and Image Processing in Biomedical Photoacoustic Imaging: A Review," *Optics,* vol. 2021, no. 2, pp. 1-24, 2021.

[59] J. Yao and L. V. Wang, "Sensitivity of photoacoustic microscopy," *Photoacoustics,* vol. 2, no. 2, pp. 87-101, 2014.

[60] B. Stephanian, M. T. Graham, H. Hou and M. A. L. Bell, "Additive noise models for photoacoustic spatial coherence theory," *Biomedical Optics Express,* vol. 9, no. 11, pp. 5566-5582, 2018.

[61] V. Perrot, M. Polichetti, F. Varray and D. Garcia, "So you think you can DAS? A viewpoint on delay-and-sum beamforming," *Ultrasonics,* vol. 111, no. March 2021, p. 106309, 2020.

[62] K. Kratkiewicz, R. Manwar, Y. Zhou, M. Mozaffarzadeh and K. Avanaki, "Technical considerations in the Verasonics research ultrasound platform for developing a photoacoustic imaging system," *Biomedical Optics Express,* vol. 12, no. 2, pp. 1050-1084, 2021.

[63] M. Mozaffarzadeh, S. A. O. I. Avanji and H. R. Jashnani, "B-Mode Photoacoustic Imaging using Linear Array: Numerical Study for Forward-Backward Minimum Variance Beamformer Combined with Delay-Multiply-and-Sum," *AUT Journal of Electrical Engineering,* vol. 51, no. 1, pp. 21-28, 2019.

[64] X. Ma, C. Peng, J. Yuan, Q. Cheng, G. Xu, X. Wang and P. L. Carson, "Multiple Delay and Sum With Enveloping Beamforming Algorithm for Photoacoustic Imaging," *IEEE Transactions on Medical Imaging,* vol. 39, no. 6, pp. 1812 - 1821, 2020.

[65] M. Mozaffarzadeh, A. Hariri, C. Moore and J. V. Jokerst, "The double-stage delay-multiply-and-sum image reconstruction method improves imaging quality in a LED-based photoacoustic array scanner," *Photoacoustics,* vol. 12, pp. 22-29, 2018.

[66] K. F. Üstüner and G. L. Holley, "Ultrasound Imaging System Performance," Mountain View, CA, 2003.

[67] M. Khosravy, N. Gupta, N. Patel and C. A. Duque, "Chapter 2 - Recovery in compressive sensing: a review," in *Compressive Sensing in Healthcare: A volume in Advances in ubiquitous sensing applications for healthcare*, Academic Press, 2020, pp. 25-42.

[68] M. Taghouti, "Chapter 10 - Compressed sensing," in *Computing in Communication Networks: From Theory to Practice*, Academic Press, 2020, pp. 197-2015.

[69] Z. Guo, C. Li, L. Song and L. V. Wang, "Compressed sensing in photoacoustic tomography in vivo," *Journal of Biomedical Optics,* vol. 15, no. 2, p. 021311, 2010.

[70] S. Qaisar, R. M. Bilal, W. Iqbal, M. Naureen and S. Lee, "Compressive sensing: From theory to applications, a survey," *Journal of Communications and Networks,* vol. 15, no. 5, pp. 443-456, 2013.

[71] Y. Zhou, J. Yao and L. V. Wang, "Tutorial on photoacoustic tomography," *Journal of Biomedical Optics,* vol. 21, no. 6, p. 061007, 2016.

[72] M. Verweij, B. Treeby, K. v. D. van and L. Demi, "2.19 - Simulation of Ultrasound Fields," *Comprehensive Biomedical Physics,* vol. 2, pp. 465-500, 2014.

[73] E. v. d. Berg and M. P. Friedlander, "SPGL1: A solver for large-scale sparse reconstruction," December 2019. [Online]. Available: https://friedlander.io/spgl1. [Accessed 18 June 2022].

[74] E. v. d. Berg and M. P. Friedlander, "Probing the Pareto frontier for basis pursuit solutions," *SIAM Journal on Scientific Computing,* vol. 31, no. 2, pp. 890-912, 2008.

[75] R. Bhavane, Z. Starosolski, I. Stupin, K. B. Ghaghada and A. Annapragada, "NIR-II fluorescence imaging using indocyanine green nanoparticles," *Scientific Reports,* vol. 8, p. 14455, 2018.